Preprint

Water Storage in Hydrous Minerals in the Shallow Martian Mantle

By

Vincent Clesi*[1,2], Rajdeep Dasgupta[1]

1 Department of Earth, Environmental and Planetary Science, Rice University, 6001 Main Street, Houston, Texas, USA

2 Institüt Für Minelarogie, Münster Universität, Correnstrasse 24, 48143 Münster

* corresponding author : v.clesi@uni-muenster.de

This version is the first version that is submitted to the journal Contributions to Mineralogy and Petrology.

This version has **not been peer-reviewed yet.**

This file includes the main text and figures, the supplementary text and figures, and the supplementary tables printed out from excel files. Each supplementary table is spread out onto two pages.

Water Storage in Hydrous Minerals in the Shallow Martian Mantle

Vincent Clesi*[1,2], Rajdeep Dasgupta[1]

1 Department of Earth, Environmental and Planetary Science, Rice University, 6001 Main Street, Houston, Texas, USA

2 Institüt Für Minelarogie, Münster Universität, Correnstrasse 24, 48143 Münster

* corresponding author : v.clesi@uni-muenster.de

Abstract

In this paper we investigate the possibility of storing water in the shallow martian mantle under water-saturated fluid absent conditions for different bulk silicate mars (BSM) compositions. We performed phase equilibria experiments on two BSM compositions with comparable Mg number for pressure between 2 and 4 GPa, temperatures between 950 to 1150°C, and for a water content of 0.3 % wt. The amphibole stability fields derived from both compositions are consistent with previous results obtained for Earth-like composition: (i) the water-saturated fluid-absent conditions expand the stability field towards higher pressures and temperature compared to fluid present conditions for both compositions tested; and (ii) the martian alkali-rich composition tend to stabilize the amphiboles at higher temperatures, as it is the case for alkali-rich Earth-like compositions. We used these results to recalculate the water storage capacity of the early martian mantle: by taking into account the possibility of amphibole crystallization in the upper mantle, the storage capacity of water in the martian mantle increases by 40 to 1000 Earth's ocean mass (400 m to 1.5 km Global Equivalent Layer) depending on the bulk composition, water content and temperature profile of the martian mantle.

1 Introduction

From many missions to the red planet (Bibring et al., 2005) it has been learned that water was present in liquid form during the early stage of Mars' history (Carr and Head, 2015; Jakosky, 2021). Mars then dried out (e;g. Scheller et al., 2021, and references therein)), and most of the remaining water is present in the polar cap (Bibring et al., 2004; Carr and Head, 2015) or as vapor in the martian atmosphere (Trokhimovskiy et al., 2015) with no liquid water left on its surface. Although a large fraction of the Martian surface water was likely lost to space (REFS), a substantial amount of water also likely got sequestered in the Martian subsurface (e.g Scheller et al., 2021). The question remains as to how much water can still be stored in the martian mantle.

It is possible to store water in the planetary mantles in Nominally Anhydrous Minerals (NAMs, Hirschmann et al., 2005; Keppler, 2006), and in hydrous minerals (Condamine et al., 2016; Fumagalli et al., 2009). Understanding the actual storage of water in a planet requires determining the total storage capacity of the mantle from NAMs and hydrous minerals. This has been done for Earth (Dong et al., 2021; Hirschmann et al., 2005) and Mars (Dong et al., 2022) using a NAM only mantle mineralogy. For Mars, this yielded a total water storage similar to global equivalent layer (GEL) of 4.9 to 9 km depending on the thermal profile.

The water storage capacity of the martian mantle would be increased by the presence of hydrous minerals in the mantle, as it is on the Earth's mantle (Ohtani, 2015). The martian mantle composition allows crystallization of amphiboles if water is present (Médard and Grove, 2006; Pommier et al., 2012), which could increase its water storage capacity. The presence of amphibole depends on their stability field, which itself depends on the composition of the mantle. It has been shown in Earth-like composition that the bulk composition controls the presence and amount of amphiboles that can form (from Mysen and Boettcher, 1975 to Saha et al., 2021 and references therein). It has also been shown that the stability of amphibole depends on the presence of H_2O-CO_2 fluids (e.g. Dasgupta, 2018; Grove et al., 2006; Mandler and Grove,

2016 and references therein). As a function of bulk water content, the dominant water storage mechanism in the mantle varies. At a sufficiently low water abundance, i.e., hundreds or ppm by weight of H_2O, and high temperatures, all water is stored in NAMs (e.g. Dasgupta, 2018; Hirschmann et al., 2005; O'Leary et al., 2010, Dasgupta and Aubaud, 2024). Similarly, too high water concentrations lead to stability of hydrous fluids or hydrous partial melts, depending on temperatures (e.g. Grove et al., 2006; Hirschmann et al., 2005; Médard and Grove, 2006; Pommier et al., 2012; Till et al., 2012), which may suppress stability of hydrous silicate minerals (Green et al., 2014, 2010). At intermediate water content of thousands of ppm, and low enough temperatures, water could be chiefly stored in hydrous silicate minerals such as amphiboles (e.g., Dasgupta, 2018; Mandler and Grove, 2016; Putak Juriček and Keppler, 2023; Saha et al., 2021; Wallace and Green, 1991).

Phase relations and melting of water-rich systems for the bulk silicate Mars (BSM) composition (Wänke and Dreibus, 1994) was studied by Médard and Grove, (2006) and Pommier et al., (2012). These studies have shown that amphiboles can be present in the martian mantle at relatively low pressures (0.5 to 2.5 GPa) and temperatures (700 to 950 °C). Because lowering the water content relative to alkalis would tend to extend the amphibole stability field toward higher temperatures and pressures, we propose to study the effect of an intermediate concentration of water (0.3% wt bulk concentration), high enough to be in the range for hydrous mineral formation, low enough to be in the absence of hydrous fluid. This concentration should extend the stability field of amphiboles from Médard and Grove, (2006) to higher pressures and temperatures, providing a higher bound for the water storage capacity in the martian mantle.

In terms of composition, the bulk concentration of alkali elements (Na and K) plays an important role in the stabilization of amphiboles and other hydrous minerals, such as phlogopites (Fumagalli et al., 2009; Mysen and Boettcher, 1975; Saha et al., 2018). Other elements, such as Ca, also controls the proportion of amphibole (Saha et al., 2021, and

76 references therein). Since the Bulk Silicate Mars (BSM) composition is not the same as the
77 Earth's mantle (Yoshizaki and McDonough, 2020), it is important to determine the stability of
78 amphibole and their proportions within the martian mantle to get a precise estimate on the
79 water storage capacity. Several BSM model have been proposed, with different Mg#, alkali and
80 Ca contents (Bertka and Fei, 1997; Lodders and Fegley, 1997; Sanloup et al., 1999; Taylor, 2013;
81 Wänke and Dreibus, 1994; Yoshizaki and McDonough, 2020). Each model will yield slightly
82 different modal distributions of mineral, (while still being comparable, see Smrekar et al., 2019
83 and references therein), and therefore different water storage capacities in the martian mantle.
84 In particular, the different models have different Na and K concentrations, and these differences
85 will affect the stability of amphiboles in the martian mantle. In particular, the model
86 composition of Lodders and Fegley, (1997) is richer in alkali material (~ 1 wt.% total Na_2O +
87 K_2O) than the one from Wänke and Dreibus, (1994; ~ 0.5 wt.% total Na_2O + K_2O), for
88 comparable Mg # (75 and 75.9 respectively) and CaO content (2.36 and 2.45 wt.%,
89 respectively). Each composition would yield different amphibole *P-T* stability fields and
90 therefore different water storage capacities in the martian mantle.

91 The goal of this study is to determine the amphibole pressure-temperature stability field

92 (*P-T* field) of two different BSM model compositions (referred as LF for Lodders and Fegley
93 (1997) and DW for Wänke and Dreibus (1994) in the rest of the paper),for a bulk water content
94 of 0.3 wt.% in experiments performed at high pressures (2 to 4 GPa) and high temperatures
95 (950 to 1150 °C) relevant to the stability field of amphibole (Mandler and Grove, 2016; Médard
96 and Grove, 2006; Saha et al., 2021). With this *P-T* stability field, we re-evaluated the total storage
97 capacity of a possibly hydrous martian mantle accounting for both model composition and the
98 thermal profiles proposed by (Samuel et al., 2021).

99

100

wt%	DW (Wänke and Dreibus, 1994)	LF (Lodders and Fegley, 1997)
SiO_2	44.67	45.65
TiO_2	0.13	0.15
Al_2O_3	3.03	2.9
MnO	0.45	0.36
FeO	18.04	17.3
MgO	30.38	29.85
CaO	2.47	2.4
Na_2O	0.5	0.99
K_2O	0.04	0.1
H_2O	0.3	0.3
Mg #	75.02	75.46
Total Na_2O + K_2O	0.54	1.09

Table 1: Composition of the starting material normalized in wt%, after decarbonation of $CaCO_3$, Na_2CO_3 and K_2CO_3 and reduction of Fe_2O_3, and addition of brucite for H_2O. The water content is calculated from the amount of brucite added during preparation. In the rest of the text, DW refers to Wänke and Dreibus (1994) composition (low alkali content) and LF refers to Lodders and Fegley (1997) (higher alkali content).

2. Methods

2.1. Experimental Procedure

2.1.1. Starting Material

The starting material consists of a mix of high purity rageant oxide powders of SiO_2, MgO, Fe_2O_3, Al_2O_3, TiO_2, MnO, mixed with carbonates $CaCO_3$, Na_2CO_3 and K_2CO_3. These oxide powders were dried and stored at 110°C prior to mixing. Each of them was weighted and mixed in ethanol using an agate mortar. The initial mixes were fired at 1000°C for 18 h under a CO-CO_2 gas-controlled atmosphere so as to achieve decarbonation of the carbonate powders and an oxygen

fugacity of FMQ -1 to reduce Fe_2O_3 to FeO. After firing, brucite [$Mg(OH)_2$] was added so as to obtain a bulk water concentration of 0.3 wt.%. Two compositions with different alkali contents and similar Mg# were synthesized: Lodders and Fegley (1997) and Wänke and Dreibus (1994), adapted without trace elements and with the addition of 0.3 wt.% of H_2O. The initial weights of each powder were determined so as to take into account the loss of mass during the decarbonation process, as well as the addition of the brucite powder, and get the compositions of starting mixes in oxide weight percentages are shown in Table 1. The powders were stored in a 110 °C controlled furnace between each experiment.

2.1.2. High P-T experiments

All experiments were conducted in Rice University's experimental petrology laboratory. The experiments at 2-3 GPa were conducted using a piston cylinder device and the experiments at 4 GPa were conducted using a Walker-style multi anvil device. For the piston cylinder experiments, a half-inch diameter $BaCO_3$ pressure cell with crushable MgO internal spacers, straight-walled graphite furnaces were used. The assembly was contained in external Pb foil, which helped to minimize friction. The *P-T* calibration and the procedural details of our piston cylinder assembly is given in Tsuno and Dasgupta (2011)and adopted in several subsequent studies from this laboratory (e.g., Carter and Dasgupta, 2015; Saha and Dasgupta, 2019; Tsuno and Dasgupta, 2012). The 4 GPa experiments were conducted using a 1100-ton hydraulic press, fitted with a Walker-style multi anvil module. We used Walker-style, 18/12 MgO castable pressure medium. The *P-T* calibration for this assembly is given in Ding et al. (2014).

The starting mixes were loaded in 2 mm outer diameter gold capsules, welded with a PUK welding machine in both ends to avoid loss of matter and contamination. The lengths of the capsules were variable (4 to 5 mm in piston-cylinder experiments, 3 mm for multi-anvil experiments). Experimental temperatures, for both PC and MA experiments were controlled by

type-C thermocouples, placed axially to the heater and within 1 mm of one end of the cylindrical capsules, and coupled with an Eurotherm temperature controller. Thermal gradients were taken into account during the entire length of the experiment both in piston-cylinder and multi-anvil experiments. The P-T uncertainties of our experiments are estimated to be ±0.1 GPa and ±12° C for PC and ±0.3 GPa and ±10°C for MA. The temperatures of study range from 950°C to 1150°C. To ensure equilibrium, piston-cylinders experiments were run for 5 days (120 hours). Multi-anvil experiments were run for 3 days (72 hours) at $T > 1050C$, to 4 days (96 hours) at $T \leq 1050C$. The conditions of experiments and their name are listed in Table 2.

For the piston-cylinder experiments, the sample were brought to the target pressure manually less than 30 minutes. For the multi-anvil experiments, the pressure was increased slowly using an hydraulic pump in 3 to 4 hours. For both multi-anvil and piston-cylinder, after the pressure was reached, the temperature was increased to the target temperature at a rate of 100 ° C per minute and kept stable at target temperature with an Eurotherm controller. After 72 to 120 hours of heating, experiments were quenched by cutting off the electrical power of the graphite heater, leading to a rapid decrease of the temperature to 100°C in less than 30 seconds. The piston-cylinder experiments are decompressed manually in 1 hour, while the multi-anvil experiments are decompressed in 15 hours by the hydraulic pump controller. Once the assemblies are decompressed, the capsules are retrieved and cut longitudinally using a 50 microns wide diamond coated saw. After being cut, the samples are mounted in epoxy and dry-polished on a nylon cloth and a 3 microns diamond powder until a flat surface is achieved. Once this flat surface is obtained, a final round of polishing is made using a velvet cloth and 1 micron diamond powder before carbon coating the sample.

2.3 Sample Analysis

After quenching, the samples were cut, polished, carbon-coated and analyzed using a field emission gun microprobe (JEOL JXA 8530F Hyperprobe) at the Department of Earth, Environment and Planetary Science of Rice University. Phase identification was performed using backscattered electron images (BSE) and Energy Dispersive X-ray Spectroscopy (EDS). The composition was determined using wavelength dispersive X-ray spectroscopy (WDS). The analysis of olivine, pyroxenes, garnet and oxides were conducted using a focused electron beam of 20 nA with an accelerating voltage of 15kV. Na-rich phases (amphiboles and melt) were analyzed with a defocused electron beam (between 5 and 20 μm depending on the available space) in the same acceleration and intensity, to limit the effet of Na migration during analysis. The calibration were performed using standard samples from the manufacturer with a known composition. For all phase types (minerals, glass and oxides), concentration of Mn and Ti were calibrated using a rhodonite and a rutile crystal, respectively. For minerals the standards used were crystals of olivine (Fe, Si and Mg), almandine (Al, Si and Fe), biotite (K), plagioclase (Na, Al and Ca), Cr-diopside (Si, Ca and Mg), and jadeite (Na). For oxides, only Fe, Al, Mg, Mn LF

and Ti were analyzed, calibrated using chromite (Fe, Al and Mg), rhodonite (Mn) and rutile (Ti). For glasses, we used different commercial glasses with known concentrations to calibrate Si, Na, K, Ca, Fe, Al and Mg, provided by the manufacturer.

The H_2O content was not directly measured in any mineral, and for amphiboles, the water content is calculated using the stoichiometric method and the spreadsheet given by (Locock, 2014) determining the molar OH/Si ratio. The H_2O content is then recalculated from this molar ratio into a percentage of H_2O (the detailed calculation is presented in Section 3.3, and the results in Tables 3 and 4).

Table 2 begin

Name	P (GPa)	T (°C)	t (h)	Capsule	Phase assembly	SSE	$K_{dMg\text{-}Fe}$ opx/ol	1σ	$K_{dMg\text{-}Fe}$ opx/cpx	1σ	$K_{dMg\text{-}Fe}$ ol/melt	1σ
LF												
T142-LF	2	950	120	Au	0.42(1) ol + 0.32 (1) opx + 0.02(1)cpx +0.24 (1) amph + sp	0.287	1.11	0.13	0.64	0.28	-	-
T143-LF	2	1050	120	Au	0.34(1) ol + 0.41(1) opx + 0.03 (1)cpx+0.19 (1) amph + sp	0.014	1.15	0.06	0.69	0.08	-	-
T146-LF	2	1100	120	Au	0.41(1) ol + 0.39(1) opx + 0.02 (1) cpx+0.18(1) amph + sp	0.198	1.20	0.08	0.73	0.42	-	-
T148-LF	2	1150	120	Au	0.48(1) ol + 0.34(1) opx +0.09(1) cpx + 0.03(1) grt + 0.06 (1) melt +sp	0.318	1.20	0.05	0.96	0.12	0.34	0.13
T150-LF	3	950	144	Au	0.43 (1) ol + 0.33 (1) opx + 0.01 (1) cpx + 0.23 (1) amph + sp	0.131	1.34	0.17	0.86	0.19	-	-
T151-LF	3	1050	120	Au	0.44 () ol + 0.37 (1) opx + 0.04 (1) cpx + 0.14 (2) amph + 0.02 (1) grt + sp	0.59	1.14	0.15	1.01	0.22	-	-
T152-LF	3	1100	120	Au	0.42 (1) ol + 0.35 (1) opx + 0.08 (1) cpx + 0.05 (1) grt + 0.10 (1) melt + sp	0.078	1.21	0.05	0.92	0.15	0.41	0.07
T153-LF	3	1150	120	Au	0.42 (1) ol +0.40 (1) opx + 0.05 (1) cpx + 0.13 (1) melt + sp	0.4	1.15	0.04	0.91	0.06	0.36	0.05
MA293	4	1050	96	Au	0.54 (1) ol + 0.23 (1) opx + 0.14 (1) cpx + 0.09 (1) grt +ox	0.333	1.28	0.08	0.91	0.16	-	-
MA297	4	1100	72	Au	0.48 (1) ol + 0.23 (2) opx +0.13 (1) cpx + 0.07 (1) grt + 0.08 (1) melt	0.344	1.26	0.08	0.70	0.23	0.41	0.07
MA300	4	950	96	Au	0.49 (1) ol + 0.28 (1) opx + 0.12 (1) cpx + 0.11 (1) grt +sp	0.505	1.26	0.05	0.83	0.09	-	-
MA302	4	1150	72	Au	0.46 (1) ol + 0.26 (1) opx + 0.08 (1) cpx + 0.08 (1) grt + 0.11 (1) melt	0.905	1.20	0.06	0.86	0.10	0.41	0.12
DW												
T142-DW	2	950	120	Au	0.50 (1) ol + 0.29 (1) opx +0.02 (1) cpx + 0.19 (1) amph + sp	0.49	1.11	0.09	0.82	0.15	-	-
T143-DW	2	1050	120	Au	0.48 (1) ol + 0.36 (1) opx +0.03 (1) cpx + 0.12 (1) amph + sp	0.64	1.22	0.18	0.88	0.18	-	-
T146-DW	2	1100	120	Au	0.51 (1) ol + 0.34 (1) opx + 0.09 (1) cpx + 0.06 (1) grt + 0.001 (100) melt + sp	1.16	1.13	0.07	0.91	0.11	0.32	0.06
T148-DW	2	1150	120	Au	0.53 (1) ol + 0.30 (1) opx + 0.10 (1) cpx +0.07 (1) grt + 0.01 (10) melt	0.16	1.12	0.10	0.94	0.21	0.35	0.05
T150-DW	3	950	144	Au	0.47 (1) ol + 0.28 (1) opx + 0.25 (1) amph +0.003 (3) grt	1.41	1.31	0.13	0.93	0.27	-	-
T151-DW	3	1050	120	Au	0.50 (1) ol +0.29 (1) opx + 0.11 (1) cpx +0.02 (1) amph +0.08 (1) grt	0.18	1.12	0.04	0.87	0.05	-	-
T152-DW	3	1100	120	Au	0.55 (1) ol + 0.26 (1) opx + 0.09 (1) cpx + 0.10 (1) grt	0.80	1.23	0.06	1.05	0.06	0.63	0.05
T153-DW	3	1150	120	Au	0.49 (1) ol + 0.35 (1) opx + 0.08 (1) cpx + 0.06 (1) grt +0.03 (1) melt	0.11	1.20	0.04	1.00	0.09	0.30	0.08
MA290	4	950	96	Au	0.43 (1) ol + 0.35 (1) opx + 0.110 (5) cpx +0.110 (3) grt	0.17	1.23	0.10	0.96	0.24	-	-
MA295	4	1050	96	Au	0.48 (1) ol +0.31 (1) opx +0.05 (1) cpx + 0.17 (1) melt	0.20	1.28	0.06	1.13	0.15	0.40	0.13
MA298	4	1100	72	Au	0.54 (1) ol + 0.11 (1) opx +0.03 (1) cpx + 0.09 (1) grt	0.21	1.38	0.08	1.28	0.70	0.42	0.15
MA303	4	1150	72	Au	0.59 (1) ol + 0.16 (1) opx + 0.09 (1) cpx + 0.09 (2) grt +0.07 (1) melt	0.38	1.27	0.08	0.98	0.14	0.50	0.12

Table 2: Tables of experimental conditions and phase assembly of the run products for composition LF and DW. The pressure are known within a ±0.1 GPa range. The temperatures are known within a 10°C range. The oxygen fugacity is not buffered during the experiments. Experiments names starting with a T (T142-LF for instance) are Piston-Cylinder experiments. Experiments names starting with MA are multi-anvil experiments. The SSE is the residual squared difference obtained after mass balance calculations. The phase proportions are presented in mass fraction. For each experiment the value of $K_{dMg\text{-}Fe}^{opx/ol}$, $K_{dMg\text{-}Fe}^{opx/cpx}$, and $K_{dMg\text{-}Fe}^{ol/melt}$ when melt is present are given with their 1σ error.

Table 2 end

190

3 Results

Figure1 begin

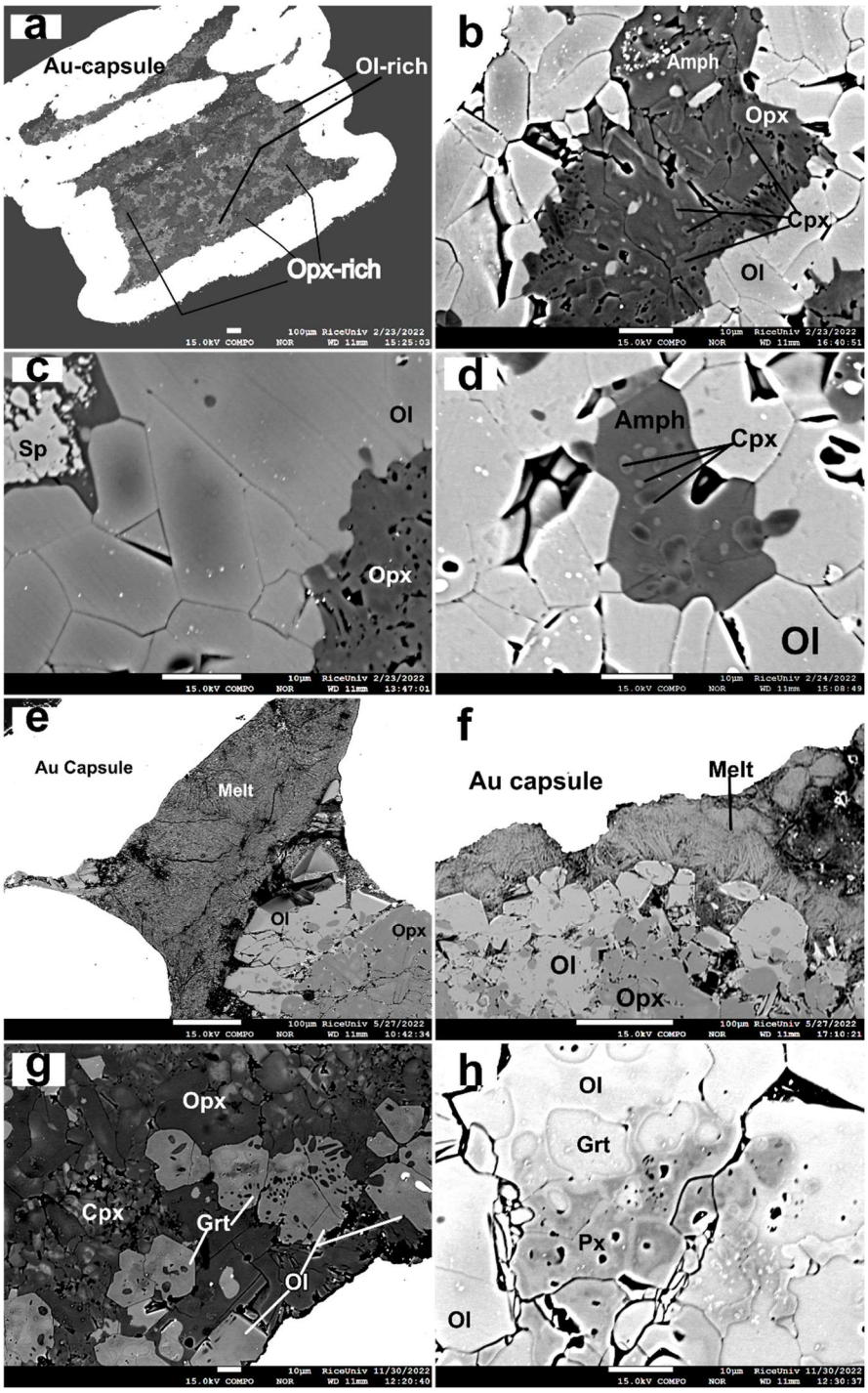

Figure 1: Backscattered electron (BSE) images of different samples showing the different textures obtained in this study. a. Whole sample image of sample T142-LF (2 GPa, 950°C). b. Detail of an opx-rich zone for sample T142-LF, showing an amphibole associated with a rim of opx and ol and the poikilitic texture with cpx. c. Details of an olivine rich zone in sample T142-LF showing the zonation of olivines at 950 °C. d. Detail of an ol rich zone for sample T143-DW (2 GPa, 1050°C) showing the disappearance of olivine zonation for temperatures above 1000°C. e. Whole sample picture of sample T148-DW (2 GPA, 1150°C) showing the presence of a melt rich area on top of the capsule. f. Detail of a melt rich area in sample T153-DW (3 GPA, 1150°C) showing the typical dendritic texture of melts obtained in this study. g. Detail of a sample MA297 (4GPa, 1100°C) showing the presence of symplectitic texture of garnets associated with ol and opx. h. Details of the symplectitic texture of a garnet on sample MA297, showing the intrication of olivine and garnets. Ol = olivines. Opx= Orthopyroxenes. Cpx = Clinopyroxenes. Grt = garnet. Px = Pyroxene (undetermined). Amph= amphiboles

Figure1 end

3.1 Approach to equilibrium

No time series experiments were performed but we are confident that equilibrium was reached in most of the experiment, following several lines of evidence. First of all, the time of our experiment is comparable with previous experiments in the same conditions (Condamine et al., 2016; Mandler and Grove, 2016; Médard and Grove, 2006; Saha et al., 2018; Saha and Dasgupta, 2019).

Secondly, from the textural analysis (see Section 3.2 and Figure 1c and 1d), only the experiments at 2 GPa and 950 °C (T142-LF and T142-DW) are not entirely equilibrated, showing some zonation in olivine (Figure 1c). This zonation disappears at higher pressures and temperature (Figure 1d), thus indicating that the duration of the experiment was enough to obtain homogeneous samples, indicating a probable equilibrium. The problem of zoning for the low temperature experiments was circumvented by using the analysis of the olivine outer rim only in this study.

The third line of evidence for equilibrium attainment, is the given by the mass balance calculation: all of the mass balance calculation have an SSE lower than one or close to 1 (Table 2) indicating the absence of elemental loss and a probable equilibrium between the phases.

Finally, the values of $K_{d\ Mg\text{-}Fe}$ between different phases (Table 2) are all comparable with previous studies where equilibrium was demonstrated. The $K_{d\ Mg\text{-}Fe}^{ol/opx}$ is comprised between 1.0 and 1.5, in the range determined by Von Seckendorff and O'Neill (1993). Furthermore, these values of $K_{d\ Mg\text{-}Fe}^{ol/opx}$ are comparable with the values of the previous study with longer experimental durations and comparable composition of Médard and Grove (2006). These values of $K_{d\ Mg\text{-}Fe}^{ol/opx}$ are also comparable to previous experimental work in volatile bearing peridotites that reached equilibrium (Condamine et al., 2016; Saha et al., 2021). The values of $K_{d\ Mg\text{-}Fe}^{opx/cpx}$ in our experiments are also comprised between 0.64 and 1.28 for all experiments, within the 0.4-1.7 range determined in previous studies for which equilibrium has been demonstrated (Condamine et al., 2016; Condamine and Médard, 2014; Mandler and Grove, 2016; Saha et al., 2021, 2018; Tumiati et al., 2013; Wallace and Green, 1991). For the experiments with melts present, all the $K_{d\ Mg\text{-}Fe}^{opx/ol}$ are in the range 0.30-0.40 when accounting

for the 1σ error, except for sample T152-DW, compatible with previous values in which chemical equilibrium has been shown (Filiberto et al., 2010a, 2010b, and references therein). The high error bars are mostly due to the fact that quenched melt with dendritic textures are complex to analyze, and not to the absence of equilibrium, which also explains the variation for sample T152-DW.

The combination of all these lines of evidence (textural, chemical and comparison with previous studies) shows that our experiments can be considered has having reached experimental equilibrium.

3.2 Texture of the run-products

We obtained BSE electron image of each sample to study the phase relationships. After recovering, the capsules did not show any trace of reaction or breaking that might have lead to contamination of the samples (Figure 1.a and 1.e). Both compositions tested present the same minerals assemblies (Table 2) and the same textures (Figure 1), with some phases appearing or disappearing sooner or later with increasing temperature and pressure.

At low temperatures (950 °C) the mineral phases are not entirely equilibrated: olivines in particular show a dark region compositionally closer to the bulk than the clearer outer rim in equilibrium (Figure 1.c). For the chemical analysis, only the equilibrated parts are presented in the rest of the paper. Despite the partial attainment of equilibrium, olivines and orthopyroxenes are crystallizing in subhedral to euhedral forms, while clinopyroxenes present anhedral crystals. The hydrous phases are subhedral amphiboles, presenting poikilitic structure with unequilibrated clinopyroxenes (white crystals inside the amphibole in Figures 1b and 1.d). The amphiboles are associated with pyroxenes forming rims around it. Surrounding the amphibole are anhedral but equilibrated cpx, themselves turning into subhedral opx.

For higher temperatures ($T \geq 1050C$), the unequilibrated zones in ol and px have disappeared. When amphiboles are present, they show subhedral crystallization and are surrounded with

anhedral cpx and subhedral opx. As temperature and pressure increase, the amphiboles disappear, being replaced by cpx, garnet and melt.

When garnets are present, they are subhedral and show symplectitic texture with opx (Figures 1g and 1h). At 3 GPa and low temperatures (950 °C and 1050 °C), both amphibole and garnet are coexisting, while at higher pressure (4 GPa, Figures 1g and 1h) or higher temperature ($T \geq$ 1050 – 1100 °C depending on composition) amphiboles disappear and garnets stay stable.

Melt was present in the higher temperature experiments, as shown by the dendritic textures shown in Figures 1e and 1f, typical of quenched melts. The quenched crystals are clinopyroxenes, with a typical width of 1 to 5 μm and lengths varying from dozens to a few hundred of microns. We did not succeed in glass quenching, and analyzed the dendritic phase with a large defocused beam larger than the size of the quenched crystal (5 to 20 microns depending on the amount of quenched melt available in the cross section).

As can be seen in Figures 1e, 1f, 1g and 1h, there is no evidence for the presence of fluids even when hydrous phases are absent. The presence of hydrous phases at low pressure and low temperature, and their disappearance at higher pressures without evidence of a fluid phase being present is strong evidence that the initial bulk water content is high enough to be water saturated (crystallization of hydrous phases) and low enough to be fluid under-saturated (no fluid or vapour H_2O present).

3.3 Minerals and melt compositions

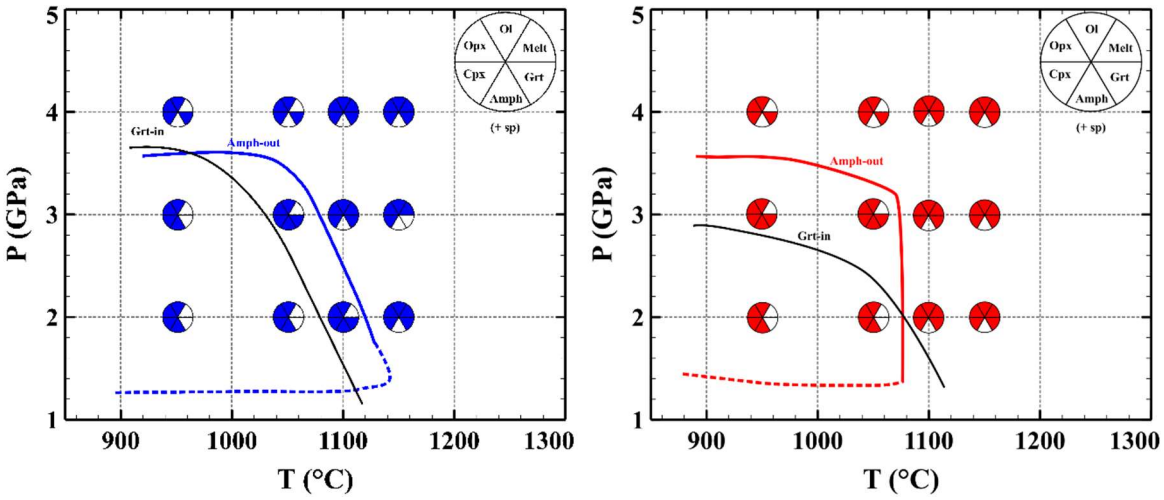

Figure 2: Phase assemblage observed in the run-products of our experiments, plotted as a function of T and P. The left panel with blue markers presents the results for LF composition. The right panel with red markerss presents the results for DW composition. The black lines in both panels mark the garnet-in boundary. The blue line (LF) and red line (DW) mark the amphibole-out boundary for each composition. On the top right of both panel are the keys for phase presence: a filled section indicate the phase is present, an empty one that the phase is absent. For both compositions spinels are present in all experiments, but not necessarily analyzed due to their size.

The phase assemblage for the range of pressure and temperature is shown in Figure 3. The main phases present for all the pressures and temperatures studied are the ol, opx, cpx, and sp. The detailed mineral and melt compositions for each experiment are presented in Table 3 to 6 in the main text, and Supplementary Table S.1 to S.8.

The olivines are 75Fo-25Fa (Tables S.1 and S.2), reflecting the Mg # of both compositions, and the high FeO content in the martian mantle compositions.

The orthopyroxene are 75% enstatites-25%ferrosilite (with negligible wollastonite contribution, 2-3%), with a small aluminium substitution on the T site (Tables S.3 and S.4). The high FeO content of martian like compositions explains the high ferrosillite contribution to the opx solid solution. The Mg# of orthopyroxene is comparable to that of olivine, reflecting the bulk Mg# of the initial compositions. Olivine and orhtopyroxene are the main bearer of Mg and Fe in the phase assembly.

The third major phase present is the clinopyroxene (Tables S.5 and S.6). The cpx are Fe-Mg rich and are in the clinoenstatite-clinferrosillite-wollastonite composition space. The wollastonite contribution is between 20 and 30%, placing the clinopyroxene in the augitic range

of composition. The Y sites of cpx are mainly occupied by Ca and Mg, but as temperature and pressure increase, Na tend to be more incorporated in the cpx. This effect is particularly visible for LF composition (Table S.5). The clinopyroxenes are the main bearer of calcium and to a lesser extent of sodium, while contributing very little to the aluminum budget.

Al-spinel is a minor phase but is present in all the samples. The spinels are usually small and associated to the olivine and garnet. Their size is varying between less than 2 μm and 5 μm for the largest ones. In most of the case, it has been impossible to analyze them in EPMA. Except for T143-DW, the spinel phase were not necessary to constrain the bulk composition in the mass balance calculations.

Garnet appears with increasing temperature and pressure in both compositions, but is appearing for significantly lower pressure and temperature in the DW composition (Figure 3). The garnet compositions (Tables S.7 and S.8) are in the almandine-pyrope-grossular solid solution with the dominant end-member being the pyrope in both composition (40 to 50 %) almandine being the second contributor (30 to 40 %) with grossular being non-negligible (10 to 20%).

The garnets combined with Al-spinel are the main bearers of aluminium when melt is absent. Garnets also contribute to the Ca budget through the grossular contribution, while less than cpx and amphiboles when these phases are present.

Amphiboles are the main sodic and potassic phase when present (Tables 3 and 4), with Na and Ca in the W site. This phase is calcic with high Fe and Mg content, putting their composition toward the pargasite end-member in the amphibole compositional space. Amphibole are hydrous amphiboles, and the calculation of water content presented in Table 3 and 4 is done by calculating the stoichiometric formula of the amphibole using the spreadsheet of Locock (2014). From this stoichiometric assignment of the element, all Si occupies the T site of the amphibole, and all of the W site is occupied by (OH)- anions. We derived the molar ratio OH/Si, and from

this molar ratio and the mass fraction of Si given by the EPMA measurement we can calulate the water content of amphibole using:

$$X_{H_2O}(\%wt) = \frac{2M_H + M_O}{M_H M_{Si}} \frac{OH}{Si} X_{Si} \qquad (1)$$

Where X_{Si} is the mass fraction of Si in wt %, M_H, M_O and M_{Si} are the molar masses of hydrogen, oxygen and silicon respectively; and $\frac{OH}{Si}$ is the molar OH/Si ratio from the stoichiometric assignment of the elements.

The W site of amphiboles being fully occupied by $(OH)^-$ anions, we get 3.8-3.9 % wt of -OH, equivalent to ~2.07 % wt of water (see Tables 3 and 4). Before melting, the presence of amphiboles is sufficient to accommodate the 0.3% wt of H_2O present in the initial bulk composition.

	T142-LF	1σ	T143-LF	1σ	T146-LF	1σ	T150-LF	1σ	T151-LF	1σ
SiO_2	46.48	0.71	44.95	0.71	44.26	0.69	47.19	1.13	46.53	0.57
TiO_2	0.39	0.14	0.45	0.12	1.09	0.23	0.35	0.04	1.22	0.18
Al_2O_3	9.33	0.66	10.45	0.52	11.79	0.37	9.59	0.89	10.62	0.70
FeO	11.11	0.91	11.23	0.24	10.55	0.77	10.53	0.53	9.33	0.27
MnO	0.19	0.04	0.19	0.02	0.21	0.02	0.16	0.01	0.19	0.02
MgO	17.16	0.66	17.41	0.24	16.94	0.28	17.51	0.51	17.38	0.56
CaO	7.91	0.73	7.86	0.54	7.84	0.23	7.87	0.59	8.48	0.40
Na_2O	3.95	0.22	3.82	0.17	3.68	0.22	4.03	0.25	3.52	0.15
K_2O	0.36	0.03	0.45	0.13	0.54	0.11	0.42	0.04	0.93	0.08
H_2O	2.05	0.03	2.09	0.03	2.08	0.03	2.08	0.05	2.09	0.03
Total	98.93		98.91		98.98		99.72		100.28	

Table 3 : Amphiboles composition for LF bulk composition. The water content is calculated using the molar ratio OH/Si considering that all Si is in the tetrahedral site, and the W-site is occupied by OH. The assignment is made using the spreadsheet from Locock (2014)

	T142-DW	1σ	T143-DW	1σ	T150-DW	1σ	T151-DW	1σ
SiO_2	44.77	0.76	43.84	0.62	46.23	0.53	45.98	0.79
TiO_2	0.49	0.11	0.59	0.28	0.33	0.05	0.61	0.15
Al_2O_3	11.20	0.68	12.41	0.47	10.21	0.72	10.66	0.33
FeO	11.37	0.58	11.42	0.22	10.30	0.88	10.66	0.21
MnO	0.20	0.03	0.22	0.03	0.19	0.03	0.21	0.03
MgO	15.97	0.34	15.89	0.47	17.63	0.48	17.10	0.36
CaO	9.29	0.35	9.23	0.17	8.07	0.66	7.22	0.66
Na_2O	3.23	0.13	3.30	0.13	3.34	0.20	4.48	0.13
K_2O	0.45	0.03	0.58	0.10	0.44	0.04	0.60	0.10
H_2O	2.05	0.03	2.05	0.03	2.06	0.02	2.07	0.04
Total	99.02		99.53		98.80		99.58	

342 *Table 4: Amphiboles composition for DW bulk composition. The water content is calculated using the molar ratio OH/Si considering*
343 *that all Si is in the tetrahedral site, and the W-site is occupied by OH. The assignment is made using the spreadsheet from Locock*
344 *(2014)*

345 When reaching the solidus temperatures (between 1050 and 1100° C depending on
346 pressure and compositions), some melt is present. For one experiment (T151-DW), there is
347 textural evidence for low grade melt, but the analysis were not possible. When analysis are
348 possible, the quenched melt exhibit high Na and K content, low SiO_2 contents and relatively high
349 MgO and FeO content, indicative of basaltic compositions (Tables 5 and 6). When melt is present
350 it becomes the main Al, Na, K and H_2O bearing-phase in the assemblage.

351

	T148-LF	1σ	T152-LF	1σ	T153-LF	1σ	MA297	1σ	MA302	1σ
SiO_2	38.77	3.74	29.38	4.34	37.99	1.51	35.81	1.96	37.09	5.35
TiO_2	1.00	0.13	1.39	0.13	0.98	0.07	1.52	0.13	1.85	0.24
Al_2O_3	11.73	1.63	8.81	1.80	11.59	0.44	8.39	0.41	6.32	1.00
FeO	14.12	1.74	15.68	0.69	14.72	0.79	12.49	0.54	15.26	0.97
MnO	0.31	0.08	0.34	0.09	0.33	0.03	0.22	0.03	0.31	0.13
MgO	8.22	1.84	11.46	0.80	9.49	0.72	9.16	0.77	12.09	2.09
CaO	7.09	2.55	7.73	3.97	8.61	0.43	2.99	0.44	5.85	3.89
Na_2O	2.84	0.26	4.21	0.41	3.69	0.29	8.00	0.98	2.70	0.83
K_2O	1.42	0.36	1.75	0.37	1.56	0.17	2.32	0.22	1.40	0.56
Total	85.50		80.75		88.95		80.90		82.87	

352 *Table 5: Melt compositions for LF starting material as obtained by EPMA.*

353

354

	T146-DW	1σ	T148-DW	1σ	T152-DW	1σ	T153-DW	1σ	MA298	1σ	MA303	1σ
SiO_2	33.97	1.71	38.31	1.08	38.21	0.10	30.27	3.27	39.71	1.91	32.05	1.54
TiO_2	0.95	0.07	0.98	0.05	1.18	0.07	1.13	0.14	1.22	0.09	0.79	0.14
Al_2O_3	10.30	0.51	10.71	0.31	9.59	0.08	11.26	1.28	10.45	1.45	6.05	0.48
FeO	15.42	1.25	15.01	0.50	14.99	0.14	16.34	0.57	12.92	1.14	14.91	1.56
MnO	0.44	0.05	0.47	0.04	0.23	0.00	0.42	0.09	0.30	0.03	0.40	0.07
MgO	7.60	0.54	8.69	0.46	14.82	0.21	8.14	1.63	9.53	2.06	13.56	1.06
CaO	9.12	0.74	8.93	0.70	2.56	0.01	10.86	1.07	3.42	1.14	6.50	1.44
Na_2O	1.80	0.61	2.46	0.22	2.04	0.01	3.39	0.79	3.35	0.55	3.83	1.62
K_2O	0.65	0.19	0.53	0.08	3.40	0.03	0.58	0.13	1.38	0.70	0.26	0.16
Total	80.25		86.09		87.02		82.38		82.27		78.36	

Table 6: Melt compositions for DW starting material as obtained by EPMA.

4 Discussion

4.1 Phase Equilibria and Chemical Reaction

From the mineral composition described in section 3.2, we determined the phase proportion of the assemblage using a Monte-Carlo based algorithm minimizing the squared standard error (SSE) to the expected bulk. The equations used in the algorithm are presented in (Li et al., 2020). In Table 2 we report the phase proportions of each experiment with the associated SSE. The main reactions of interest in our study are the one composing the amph-out boundary shown in Figure 2. For each composition, there is two ways of destroying amphiboles: increasing the pressure at a constant temperature (isothermal reaction) and increasing temperature at a constant pressure (isobaric reaction).

When considering the isothermal reaction, we note that the modal shares of garnet, clinopyroxene and olivine are increasing when crossing the amphibole-out boundary at 950°C, combined with an increase in Na concentration in the clinopyroxenes and a of Ca concentration in garnet. This indicates that formation of amphibole (main bearer of Na and Ca at lower P for this temperature) at low temperature happens by destruction of clinopyroxene, garnet and olivine. The crystallization of amphiboles at low temperature (i.e. when melt is not present) can be calculated using experiments MA300 and T142-LF for the LF composition:

$$0.31\ \mathrm{ol} + 0.4\ \mathrm{cpx} + 0.48\ \mathrm{grt} + 0.02\ H_2O \leftrightarrow 0.19\mathrm{opx} + \mathrm{amph} \qquad (2)$$

where the coefficients are calculated from the mass fractions in Table 2 and normalized for 1% wt of amphibole. For the DW composition the equation is almost the same, except Mg and Fe in the amphiboles are provided by pyroxene rather than olivine. Using MA290 and T142-DW we get:

$$0.34\ \text{opx} + 0.47\ \text{cpx} + 0.59\ \text{grt} + 0.02\ H_2O \leftrightarrow 0.40\ \text{ol} + \text{amph} \qquad (3)$$

with all the calculation done in %wt from the mass fraction in Table 2, normalized to 1% wt of amphibole. Reaction 2 is comparable to the reaction determined by Médard and Grove (2006) for lower temperatures, and with comparable coefficients. As for reaction 3, the creation of olivine instead of orthopyroxene might be explained by larger error bars on the measurements (SSE are higher for DW than LF, Table 2) and by the fact that olivine and orthopyroxene are acting both as Mg and Fe donor. In all cases the amount of water needed to crystallize one mass unit of amphiboles is much lower than the bulk 0.3% wt in our experiments.

The other reaction in amphibole out boundary is along isobaric paths and is a melting reaction (i.e. the amphibole out boundary is the same as the solidus of the composition). Experiment T146-LF and T148-LF are on each side of the solidus and we get the following melting reaction (normalized to 1 % wt of melt production):

$$2.84\ \text{amph} + 0.82\ \text{opx} \leftrightarrow 1.15\ \text{ol} + 1.08\ \text{cpx} + 0.44\ \text{grt} + \text{melt} \qquad (4)$$

where everything is normalized to the creation of 1% wt of melt. For DW composition, the experiments performed at 3 GPa are more suited to calculate the melting reaction (better SSE, see Table 8). Experiments T152-DW and T151-DW are on each side of the solidus, and by difference we get:

$$4.28\ \text{amph} + 8.20\ \text{opx} + 4.08\ \text{cpx} \leftrightarrow 12.65\ \text{ol} + 2.93\ \text{grt} + \text{melt} \qquad (5)$$

all normalized to the creation of 1%wt of melt.

The water present in the amphibole is then transferred to the melt which has a much higher solubility (~3-4 % wt according to Mitchell et al. (2017), or even up to ~6-7 wt % for Lesne et

401 al. (2011)) at the conditions of our experiments, thus explaining the low totals in Table 5 and
402 6.

403 In the rest of the text, we will focus on isothermal reactions (Equation 2 and 3) to model the
404 creation of amphibole within the martian mantle.

405 4.2 Stability field and modal proportion of amphiboles

406 From the phase relations presented in Figures 2 and 3 and Tables 3.3 and 8, we determined the
407 P-T stability fields of the amphiboles for our compositions, shown in Figure 3. The lines are
408 drawn using a quadratic interpolation between the data points presented in Figure 2. Figure 3
409 shows that amphibole stability fields behave in the same for BSM composition and Earth's
410 mantle compositions. In particular our DW composition is close to the Médard and Grove
411 (2006) composition, with lower water content. As can be seen in Figure 3, lowering the water
412 content expands the amphibole stability field to higher pressure and temperature, which is the
413 same effect as on Earth-like composition. Furthermore, the two compositions presented in
414 Table 1 differ mostly by their concentration in alkalis (Na and K) elements. The LF composition
415 has more alkali element than DW, and the stability field of amphibole for LF composition is

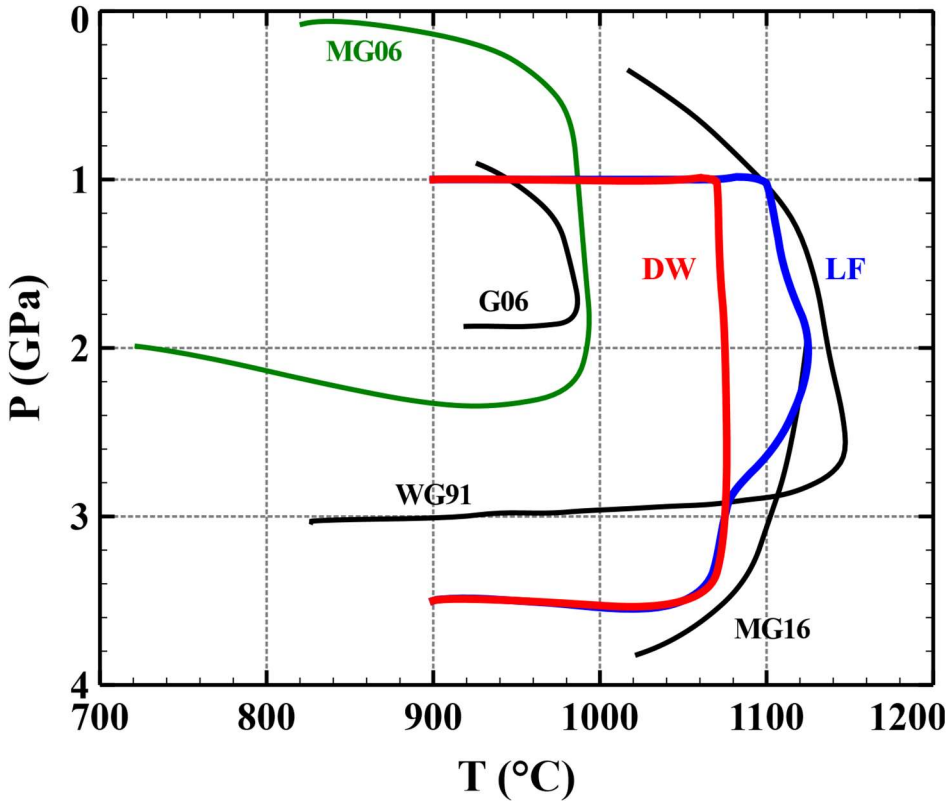

Figure 3: Amphibole stability field in the pressure temperature space. The red line is the stability field for DW composition extrapolated from Figure 2. The blue line is the stability field for LF composition extrapolated from Figure 2. The green line MG06 is the stability field determined by Médard and Grove (2006), for 3%wt of H_2O and a bulk composition close to DW composition. The black lines are the stability field determined for water-saturated-fluid absent condition in Earth-like composition. G06:Grove et al. (2006) WG91: Wallace and Green (1991) MG16: Mandler and Grove (2016)

spanning larger range of temperature, especially at 2 GPa. This shows that for martian-like compositions, increasing the total alkali bulk concentration tends to favor amphibole stability toward higher temperatures and pressures. This effect of composition on the P-T stability field is also translated in the modal composition: alkali-rich compositions tend to present higher modal fraction of amphiboles for the than the same P-T conditions. In our case, the LF compositions crystallize 22 to 23 %wt of amphibole in the P-T stability space, while DW present 15 to 20 %wt in the stability space.

All things considered, the results presented in this study are compatible with previous results obtained for Earth-like composition: effect of Temperature (Green et al., 2010; Saha et al., 2018), fluid saturation (Mandler and Grove, 2016), bulk composition (Saha et al., 2021, and references therein). This proximity we previous study means that we can then use previous work alongside ours to determine a statistical relationship in order to determine the modal fraction of amphibole as a function of composition, pressure, temperature and $\frac{Na_2O+K_2O}{H_2O}$ ratio.

By using the database in the supplementary data of Saha et al. (2021), we can parameterize the modal concentration of amphibole following:

$$\%\mathrm{wt}_{amp} = \Sigma_{i \neq Na,K} a_i \chi_i (\%wt) + \mathrm{bT} + \mathrm{cP} + \mathrm{d}\frac{\chi_{Na_2O} + \chi_{K_2O}}{\chi_{H_2O}} \quad (6)$$

with $\%wt_{amph}$ being the modal fraction of amphibole in % wt, b the effect of T in $\%wt.^{\circ}C^{-1}$, c the effect of P in $\%wt.GPa^{-1}$, a_i the effect of element i for each element present in the composition except Na, K and H_2O and d the effect of the alkali over water ratio in $\%wt$. The details of the parameterization are presented in Supplementary section S1 and the value of the parameter is given in Table 7. This parameterization is purely numerical and used to fit the data only when amphibole is present: there is no parameterization on the extent on the P-T stability space. We use a reduced dataset from Saha et al. (2021) augmented by our data for experiments where amphibole is present. Equation 6 predicts the modal share (in % wt) of amphibole when amphiboles are present, as shown in Figure 4. As shown in Figure 4, the prediction is good except for a few points where the amphibole modal fraction is higher than 30 % wt.

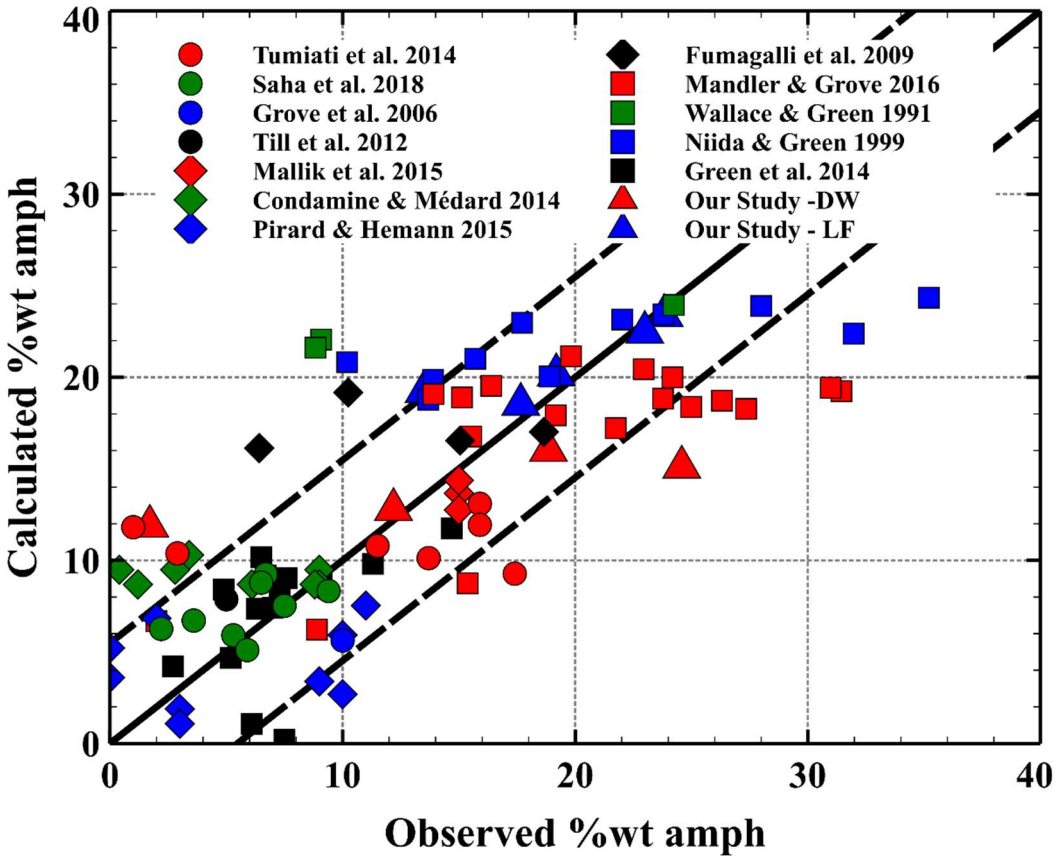

449

450 *Figure 4: Figure presenting the calculated modal share of amphiboles as predicted by equation 5 compared to the actual*
451 *observed modal shared. The solid black line is the 1:1 line and the dashed black lines are the 2σ variation. After 30% wt of*
452 *observed amphibole modal share, the model is significantly less precise. Data are from: Condamine and Médard (2014);*
453 *Fumagalli et al. (2009); Green et al. (2014); Grove et al. (2006); Mallik et al. (2015); Mandler and Grove (2016); Niida and Green*
454 *(1999); Pirard and Hermann (2015); Saha et al. (2018); Till et al. (2012); Tumiati et al. (2013); Wallace and Green (1991).*

455

Parameter	Value
$aSiO_2$	2.76
$aTiO_2$	62.30
aAl_2O_3	-11.79
aCr_2O_3	4.55
$aFeO$	0.07
$aNiO$	-51.85
$aMnO$	-47.90
$aMgO$	-1.75
$aCaO$	11.63
aP_2O_5	-50.84
aCO_2	-1.29
b	-0.03

c	-0.91
d	-1.4

Table 7: Table of the parameter value for Equation 6. The parameters value were obtained by fitting the observed %wt from the dataset from Saha et al. (2021) The results of the fitting are presented in Figure 4.

4.3 Thermal model of martian mantle and modal composition of martian mantle

In order to estimate the water storage capacity, one has to evaluate the modal proportion of each phase in the martian mantle (Dong et al., 2022). In our case, we differ from previous studies by combining the NAM's modal distribution (such as Dong et al. (2022), Bertka and Fei (1997) or Sanloup et al., (1999)) with hydrous minerals (in our case amphiboles), without saturation (contrary to Médard and Grove, 2006; Pommier et al., 2012) and therefore without lettered phase at high pressure. All modal proportion model in dry set-up are comparable (Smrekar et al., 2019), therefore the main problem is to calculate, in a fluid absent-water saturated martian mantle, how much amphiboles can crystallize. This amount is dependent on pressure, temperature and composition, as shown in Section 4.2, so we define the aerotherms for which we calculate the modal distribution of minerals to capture the effect of P and T in the martian mantle as well as the effect of composition

To test the difference between high temperature and low temperature, we chose the aerotherms from Samuel et al. (2021) (Figure 5). This study presents a 'cold' thermal profile close to one of the adiabatic profiles that was used in Dong et al. (2022) study, and a 'hot' thermal profile taking into account a high density 500 km thick layer at the martian core mantle boundary.

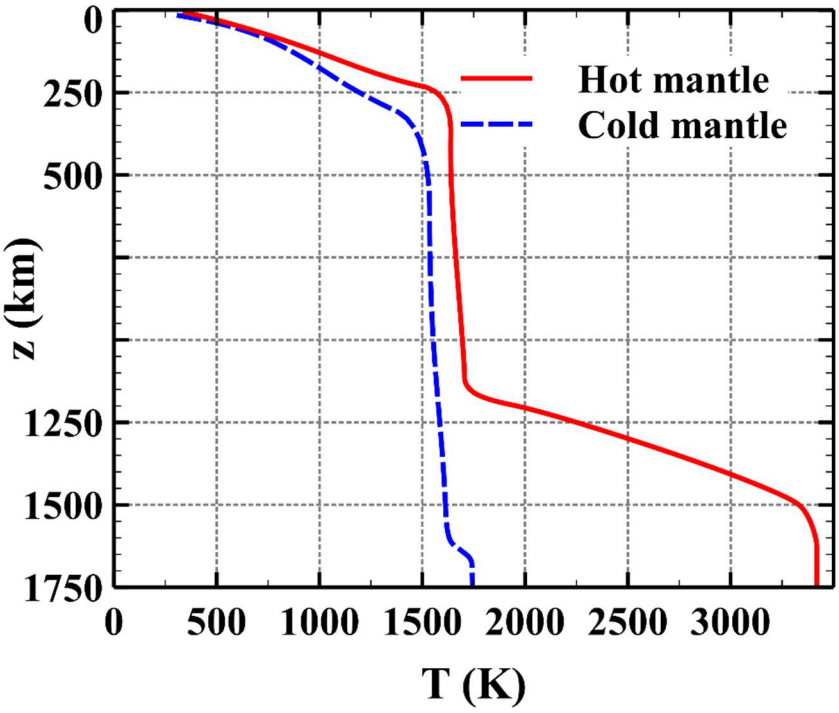

476

477 *Figure 5: Thermal models of Samuel et al. (2021)used in this study. The red solid line is the 'hot' mantle, determined by the*
478 *existence of a thermal exchange layer at the Martian Core-Mantle-Boundary. The blue dashed line is the 'cold' mantle, closer to*
479 *an adiabatic gradients of Dong et al. (2022). The pressure associated with z is calculated using the hydrostatic equation and the*
480 *mean density and thicknesses provided in the Samuel et al. (2021) study*

481 This layer concentrates the heat producing elements which leads to a hotter present-day
482 mantle. Each thermal profile represents two end-member scenarios, one cold and one hot with
483 a sharp increase of temperature at 1200 km depth, which leads to higher temperatures at
484 shallower depths. We then have a relationship $z = f(P,T)$ (Figure 5) for which we can determine
485 for each compositions (LF and DW) where amphiboles are present and how much amphiboles
486 are present using Equation 6.

487 The phases assembly presented in Tables 2 does not cover the full range of martian mantle
488 pressures, so it must be completed for pressures higher than 4 GPa and lower than 2 GPa. The
489 model of Dong et al. (2022), based on the thermodynamical modeling is complete but
490 complicated to adapt for temperature profiles different from adiabatic profiles. Most of the
491 mineralogical model are not that different from each other, and emphasize the larger role of
492 olivine polymorph and orthopyroxenes compared to Earth (Smrekar et al., 2019). The
493 differences lie in the amount of stishovite and Ca-perovskite (5% max for (Sanloup et al. (1999),
494 0% for (Bertka and Fei (1997)).). Since even in the best case those phases are minor water

bearers (few hundreds of ppm at best, Dong et al. (2021)and references therein) and they do not take up a significant modal share susceptible to affect the results. We use the simple model of Bertka and Fei (1997) that neglect these minor phases, therefore we do not introduce a large error in the estimation of the water storage capacity of the martian mantle.

When the thermal profile crosses the amphibole stability field, we use Equation 6 to calculate the modal share of amphiboles for a given water content. The modal shares of the other minerals are calculated from the amphibole modal share determined by Equation 6, using the Bertka and Fei (1997) at higher pressure as a starting point and applying Equation 2 for LF composition, and Equation 3 for DW composition. We obtain for Each composition and each thermal model the modal distribution in Mars's mantle for a given bulk content of water, with an example shown in Figure 6 for 0.3% wt of water.

4.4 Water storage capacity per phase

From our results, we can determine the concentration of water in amphiboles using Equation **6**. In both compositions, amphiboles hold between 2.05 and 2.09% wt of H_2O (Tables 3 and 4), and their mean values is similar for both compositions (2.08±0.17 and 2.06±0*12* %wt,for LF and DW respectively), therefore we use $c^{amph}{}_{H_2O} = 2.07\%wt$ in the formulas hereafter.

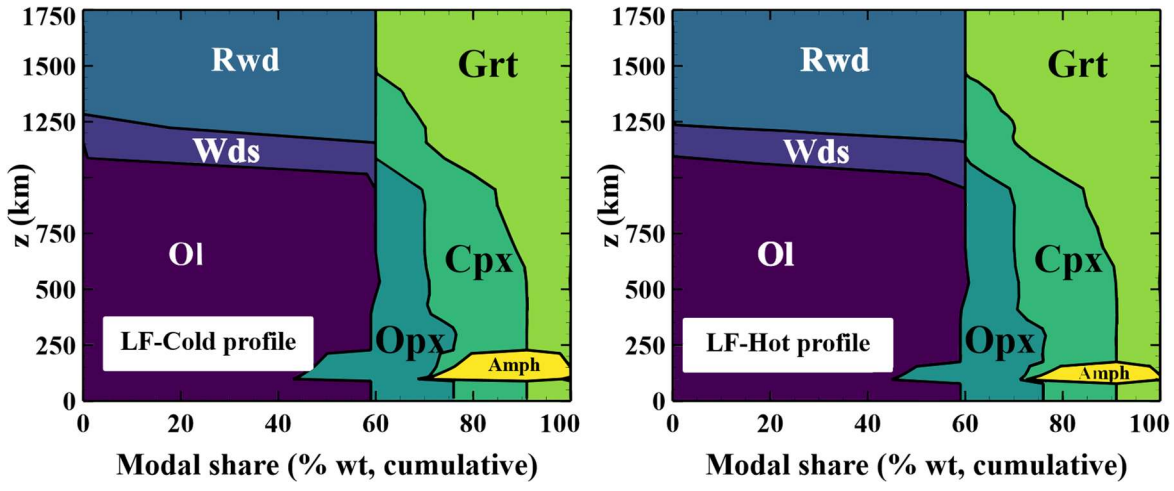

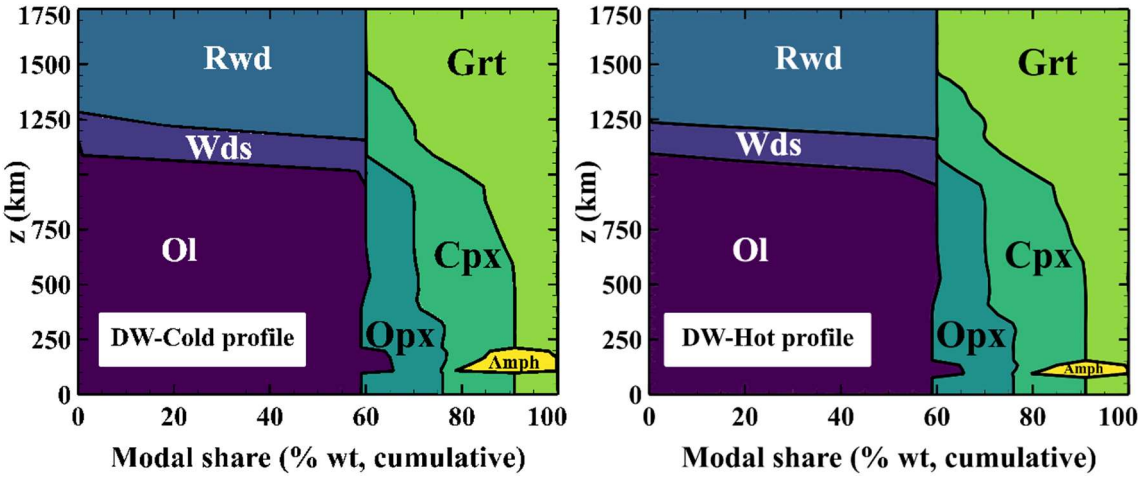

512

513 *Figure 6: Modal distributions of the different species as a function of depth in the martian mantle for LF composition (top row)*
514 *and DW composition (bottom row). The left column shows the 'cold' thermal profile of Samuel et al, (2021). The right column*
515 *shows the 'hot' thermal profile (thermal boundary layer at the CMB) from Samuel et al. (2021). All profiles are calculated for a*
516 *bulk water content of 0.3% wt.*

517 The capacity of NAM's are calculated using the formula of Keppler (2006) modified by Dong et
518 al. (2021). The main bearer of water in NAMs are olivines, and at higher pressures wadsleyite,
519 then ringwoodite. The concentration of water in the olivine polymorphs is given by:

520 $$c_{H_2O}ol = \frac{n}{2}\ln f_{H_2O} + \frac{b_{ol}}{T}$$

521 (7)

522 And

523 $$c_{H_2O}wds, rwd = a_i + \frac{b_i}{T} \qquad (8)$$

524 where the subscript *i* indicates the name of one of the olivine polymorphs (ol, wds or rwd). The
525 parameters used in these equations are the ones given by Dong et al. (2021) and Dong et al.
526 (2022). In Equation 7, we have $n = 0.6447 GPa^{-1}$, and $b_{ol} = 4905.5403 K^{-1}$. The water fugacity f_{H2O}
527 is calculated using the formula and code used in Hirschmann et al. (2005) . As explained in Dong
528 et al. (2021), the concentration of water in wadsleyite and ringwoodite is independent of the
529 water fugacity. Therefore, the water fugacity term of equation 7 is replaced by a constant a_i in
530 Equation 8. In this case, the parameter's values are different for wadsleyite and ringwoodite.
531 We have $a_{wds} = 7.6356$ and $b_{wds} = 13739.5371 K^{-1}$ for wadsleyite, and $a_{rwd} = -6.8856$ and $b_{rwd} =$
532 $12206.2676 K^{-1}$.

The water concentration of the rest of the NAMS is set by the partitioning coefficients of water between olivine polymorphs and the other phases (see Dong et al., 2021; Hirschmann et al., 2005; Keppler, 2006 for more details on the thermodynamics of water storage in NAMs). The partitioning coefficient is given by:

$$D_{H_2O}\mathrm{i/j} = \frac{A_i}{A_j} f_{H_2O}^{n_i - n_j} \exp\left(-\frac{(\Delta H_i - \Delta H_j) + (\Delta V_i - \Delta V_j)P}{RT}\right) \quad (9)$$

where *i* stands for one of the olivine polymorphs and *j* for one of the other NAMs present. R is the ideal gas constant, P is expressed in Pa and T in Kelvins. In our case, the NAMs are opx, cpx and grt. The value of the parameters A, n ΔH and ΔV are taken from (Keppler, 2006) and

Phase	$A(ppm.bar^n)$	n	ΔH $(kJ.mol^{-1})$	ΔV $(cm^3.mol^{-1})$
ol polymorph	0.0066	1	0	10.6
cpx	7.144	0.5	0	8.19
opx	0.042	0.5	-79.685	11.3
grt	0.679	0.5	0	5.71

Table 8: Values of the parameter used in Equation 9. The determination of the value was made in (Keppler, 2006). The olivine polymorphs share the same values

presented in Table 8. The water concentration in NAMs is then calculated by $c_{H_2O}^{j} = \frac{D^{i/j}}{c_{H2O}^{i}}$. The total water storage capacity at any given depth is therefore given by:

$$c_{H_2O}^{total}(z) = \Sigma_i \chi_i(z) c_{H_2O}\mathrm{i}(z) \quad (10)$$

where $\chi_i(z)$ is the modal proportion of mineral i at depth z and $c^i{}_{H2O}(z)$ is the concentration of water in mineral i at depth z. $\chi_i(z)$ is calculated following the procedure described in section 4.3. An example of the type of profile Equation 10 yields is presented in Figure 7 for a bulk initial concentration of 0.3% wt H_2O. Figure 7 shows the shape for all case studied here: close to the

surface, NAMs, especially cpx, are able to store more water than at lower depths reaching a storage capacity close to 1% wt. At higher depth ($\sim 1000km$ and above), wadsleyite replaces olivine and its storage capacity is higher, leading to higher values of $c_{H_2O}^{total}(z)$. When wadsleyite is transformed into ringwoodite ($z > 1250km$) the storage capacity of water gets lower, thus leading to a decrease in the value of $c_{H_2O}^{total}(z)$ compared to the wadsleyite layer. This profile is close to the one proposed by previous studies on NAMs (Dong et al., 2022; Hirschmann et al., 2005), but differs by the presence of an amphibole riche layer. This amphibole rich layer is deeper than the crust, and its extent varies with composition and thermal profile: LF composition yields a 97.5 km to 139 km thick layer for hot and cold mantle respectively, while DW composition yield a 78 km to 115 km thick layer for hot and core mantle respectively. This amphibole rich layer increases locally the water storage capacity. The extent of this increase is dependent on the modal fraction of amphibole, which is also controlled by the temperature and composition (Equation 6), which explain why in the cases presented in Figure 7 the peak in water storage for the amphibole rich layer is 0.55 %wt for LF composition while it is 0.35% wt for DW compositions. The thickness and height of this peak are the main controls in the in the variations of the bulk storage capacity. The thickness and position of the peak depend on the thermal model which controls the stability field of amphibole (Figure 4) and the amount of amphibole present (Equation 6). The height is dependent on the thermal model and bulk composition: DW composition tend to have a smaller stability field (Figure 4) and a maximum amount of amphiboles lower than LF composition (Table 2), as well as a smaller alkali over water ratio (Equation 6).

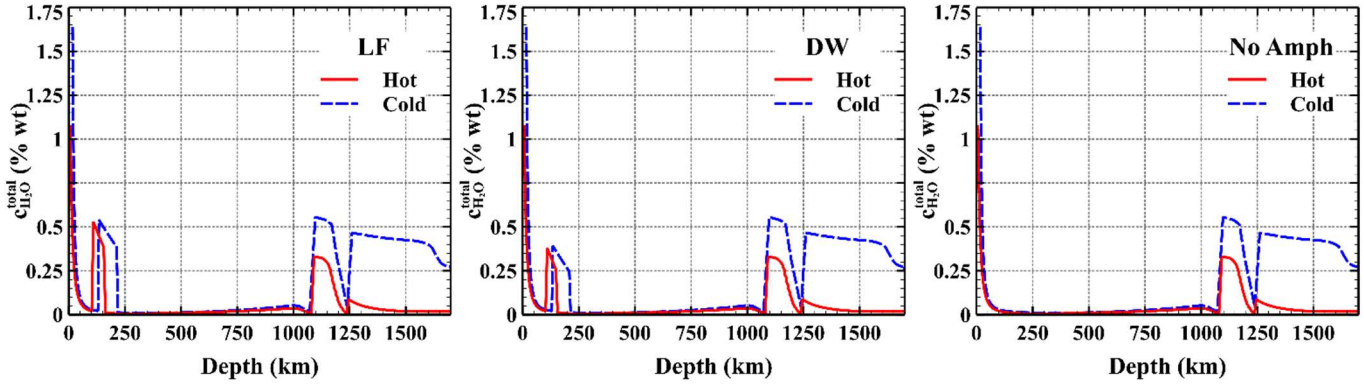

Figure 7: : Water storage capacity of Mars mantle for LF composition (left), DW composition (center) and without amphibole (right). On the three panels, the solid red line is the hot model from Figure 5 and the dashed blue line is the cold model from Figure 5. Each model is calculated for a bulk water concentration of 0.3% wt. The modal fraction of mineral is presented in Figure 6 for LF and DW composition, the modal fraction of mineral without amphibole is the model of (Bertka and Fei, 1997). The water concentration is given by Equation 10.

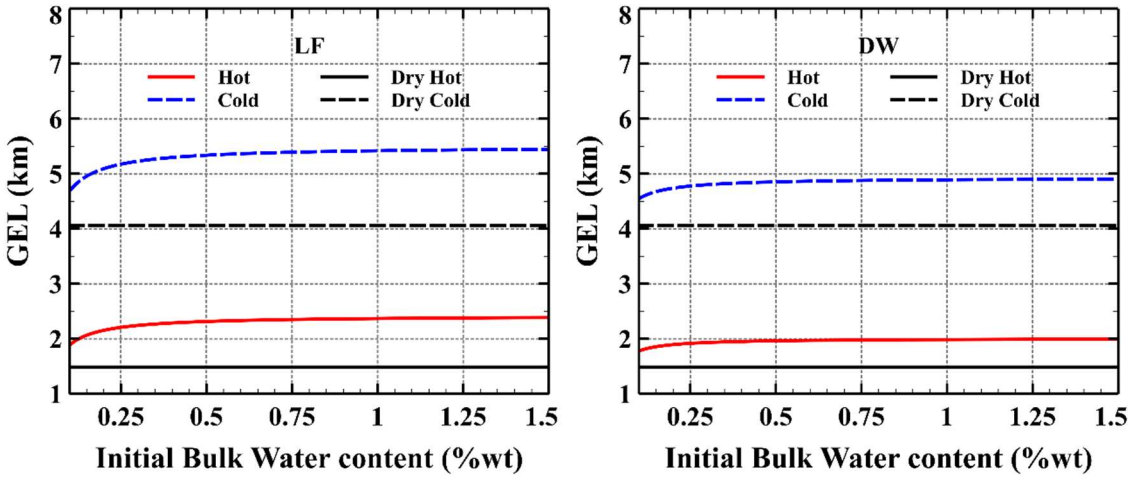

Figure 8: Evolution of water storage capacity expressed in Global Equivalent Layer (GEL) thickness in km for LF composition (left) and DW composition (right) as a function of martian mantle bulk water content (in %wt). The red solid lines are the storage capacity for a hot mantle, the blue dashed line for a cold mantle. The Bertka and Fei (1997) model with no amphibole is shown in black and shows a water storage capacity of 1.5 km for a hot mantle (solid black lines) and 4 km for a cold mantle (dashed black lines). 1 km GEL corresponds to a total water mass of 107 Earth's oceans mass. variation of the total water storage capacity

4.5 Water storage capacity of Mars

With Equation 10, we can then calculate for each of our composition the water storage capacity profile within Mars. In Figure 7 is presented an example of the evolution of $c_{H_2O}^{total}(z)$ for each composition and thermal profile for a bulk water content in the Martian mantle of 0.3% wt. Integration of these profiles over the depth of the martian mantle can yield the bulk capacity of water storage in the BSM in the form of a water concentration. If we consider that the P-T stability field of amphibole in Section 4.2 determined for a bulk water content of 0.3% wt by our experiments can be representative of the P-T stability field for all the water concentration

below fluid saturation, we can extrapolate and calculate the total water storage capacity for BSM bulk water content varying between 0.1% wt and 1% wt. In Figure 8 we present the bulk storage capacity for both BSM composition as a function of the bulk content of water. The same calculation for a non-amphibole profile yields a storage capacity equivalent to a GEL of 1.5 and 4 km for hot and cold mantle respectively. Compared to Bertka and Fei (1997) mineralogy, our amphibole bearing models (LF and DW composition) yield the water storage capacities between 1.5 km and 4 km GEL depending on the composition, water content and thermal model.

Figure 8 shows the total storage capacity increases with increasing bulk content of water. This is essentially by stabilizing amphiboles toward a higher modal fraction. However, this increase reaches quickly a maximum storage capacity for bulk water content of 0.5% wt in both compositions. This may be due to the fact that we did not explore the full effect of water content on the P-T stability field: increasing the bulk concentration toward a fluid present situation would change the P-T stability of amphibole toward lower P and T, as shown by the results of Médard and Grove (2006). Further studies and better parameterization of the effect of water content on the amphibole-out boundary are necessary to get a full view of the bulk capacity. For a given composition and thermal model, this increase is limited: increasing the bulk content of water from 0.1 % wt to 1%wt only increase the GEL thickness from 4.6to 5.45 km for LF composition and cold model, i.e. a ~1 km GEL increase (around 100 Earth's Ocean mass of water). In the case of the cold DW composition scenario, the same variation in the bulk content of water yields an increase of 200 m GEL in the total water storage capacity (from 4.6 to 4.8 km GEL). The variation of storage capacity with increasing bulk water content is even less important in the hot mantle scenarios described in Figure 8: increasing water content leads to an increase of 200 m GEL in the water storage capacity for DW composition (from and 1.78 to 1.98 km GEL) and an increase of 500 m GEL for LF composition (from 1.9 to 2.4 km GEL).

The water storage capacity is affected by the total alkali content in a comparable way as it is by the bulk water content. The alkali-rich composition LF yield, for a given thermal profile, a higher

water storage capacity than the alkali poor composition DW: for hot mantle the storage capacity is varying between 1.9 and 2.4 km GEL for LF while it is varying between 1.8 and 2 km GEL for DW; and for cold mantle the LF composition varies between 4.6 and 5.45 km GEL for LF and between 4.55and 4.9 km GEL for DW. This means that the choice of alkali-rich composition over an alkali poor composition lead to an increase of 200 to 700 m GEL in total water storage capacity for hot and cold mantle respectively. This effect is predictable from a higher modal share of amphiboles (Equation 6) combined with a larger P-T range of stability. The main control of the water storage capacity is the thermal model: hotter mantle tends to stabilize less amphiboles, and therefore store less water at depth. Furthermore, the NAMs, especially olivine and wadsleyite, are sensitive to temperature and their water storage capacity is decreased by increasing temperature (Equations 7 and 8). The hot mantle in our case yields a 1.8 to 2.4 km GEL for alkali rich composition LF, and between a 1.8 and 2 km GEL for alkali poor composition DW, which correspond to ~180-240 and ~190-200 Earth's ocean mass for LF and DW respectively. The cold mantle profile yields a total water storage capacity of 4.5 to to5.5 km GEL for LF and 4.5 to 4.9 km GEL for DW, which correspond to ~470-550 and ~450-490 Earth's ocean mass for LF and DW respectively.

The hot mantle results are significantly less than the lowest estimates of Dong et al. (2022) models (~4.9 km GEL for comparable aerotherms), while the cold mantle results are comparable to their high temperature models. This is due to Dong et al. (2022) model taking into account the temperature for wadsleyite formation, and having a more extended wadsleyite stability field at higher pressure than in the Bertka and Fei (1997) modal distribution chosen here: the amphibole-free modal distribution yield a GEL of 1.5 km for the hot model, and 4 km for the cold model. Since wadsleyite is the main bearer of water in NAMs at high pressure (responsible for the peaks around 1100 km in Figure 7), the overall water storage capacities of the martian mantle in our models are lower than Dong et al. (2022) estimates. In any case, the total water storage capacity in our models are much over the estimates of 1000-1500 m GEL of liquid water present at the surface of Mars (e.g. Filiberto et al., 2016), thus confirming the fact

647 that most of the martian water can be either degassed or stored into mantle and crust mineral
648 (Dong et al., 2022; Scheller et al., 2021; Wernicke and Jakosky, 2021).

649 4.6 Implications for martian mantle present state and history

650 Stable amphiboles within the martian mantle can increase the storage capacity of the martian
651 mantle, especially in the upper mantle area between 70 and 250 km (Figure 7). In this section,
652 we will discuss if it is possible that this amphibole-rich layer is actually present in the martian
653 upper mantle. We will then discuss what are the implications on the water initial budget of
654 Mars, and how the stability field of amphiboles affects the volcanism on Mars.

655 4.6.1 Existence of an amphibole-rich layer on Mars current mantle

656 The existence of an amphibole-rich layer can be observed in the martian mantle because
657 amphibole tend to decrease of S-wave velocities (Saha et al., 2021). The study of Saha et al.
658 (2021) showed that adding 10% to 20 % of amphibole in peridotite mantle would lower the S-
659 wave velocity v_S by 1 to 1.5 %, from 4.5 km.s^{-1} to ~ 4.3-4.4 km.s^{-1}. From our results, the presence
660 of amphiboles in comparable amounts whould be betweeen 70 and 250 km depth, and therefore
661 the S-waves velocity on Mars should be decreased by the presence of an amphibole-rich layer.
662 From the InSight data, Khan et al. (2021) reconstructed the seismic waves velocity profile of
663 Mars' upper mantle. Their profile shows that v_S are comprised between 4.2 and 4.5 km.s^{-1} at 100
664 km depth and between 4.4 and 4.6 km.s^{-1} at 250 km depth. This range is compatible with the
665 presence to some extent of amphiboles without phlogopites, provided that the seismic
666 attenuation due to amphibole in Earth peridotite (Saha et al., 2021) is the same on Mars. On the
667 other hand, the absence of a sharp discontinuity in Khan et al. profiles for these depths are an
668 indicator that, if present, the amphibole-rich layer is not part of a martian transition zone. In
669 any case, it is impossible to confirm or infirm the presence of such a layer in the martian mantle
670 for the depths between 100 and 250 km with the current martian seismic data. Between 70 and

100 km the seismic data are even more complex to untangle, with velocities ranging from 4.1 to 4.6 km.s^{-1}, and the beginning of the transition zone from mantle to crust inducing a decrease of v_S. In this area, the presence of amphiboles could account for part of the v_S decrease observed by Khan et al., although it might be hard to distinguish from the crust/mantle transition around 72 km depth (Knapmeyer-Endrun et al., 2021).

If the presence of an amphibole rich-layer is confirmed, then it will have to be taken into account when calculating the thermal history through relaxation (Samuel et al., 2019) given the documented effect of amphibole in the mantle rheology on the Earth (Green et al., 2010; Kovács et al., 2017). Confirmation of the presence of an amphibole-rich layer could provide more constraints on the drying scenarios of Mars (Scheller et al., 2021), as well as re-evaluating the water reservoirs distribution of the martian mantle (Barnes et al., 2020; McCubbin et al., 2016).

4.6.2 Possibility of ancient amphibole rich layer

There is evidence for Mars to accrete some water (Brasser, 2013; Breuer et al., 2016; Dreibus and Wänke, 1987; Khan et al., 2022), and for water to be present during the early stage of Mars(Kurokawa et al., 2014). The crystallization of amphibole and long-term storage of water is possible if the water is retained in the mantle, and if the mantle is cooling fast enough. The initial bulk content of water in the BSM is somewhere between 0 and ~ 3 – 4 % wt, depending on the estimation methods. The models favoring simple mixing between on dry reduced component from the inner solar system and one water-rich and oxidized component from the outer solar system tend to estimate high water contents, above 3 % wt(Clesi et al., 2016; Dreibus and Wänke, 1987). On the other hand, models favoring accretion from inner solar system planetesimals tend to estimate low water contents on Mars, below 0.5 % wt (Brasser, 2013; Lunine et al., 2003). The overall range is enough for amphiboles to be present, as long as the bulk content is above 0.1% wt, which seems to be the case. In the early days of martian history it is probable that the planet underwent a magma ocean stage (Elkins-Tanton, 2008; Schaefer and Elkins-Tanton, 2018). For amphiboles to be able to crystallize, the initial content

697 of water has to be retained in the upper mantle through the magma ocean crystallization. If this
698 crystallization is made at equilibrium and some interstitial melt is present, then 70 to 90 % of
699 H can be retained in the mantle (Maurice et al., 2023). This phenomenon would provide enough
700 water for amphibole crystallization in the martian upper mantle: with 0.1 (Brasser, 2013) to
701 3% wt (Dreibus and Wänke, 1987) of water during the magma ocean phase and 70% to 90% of
702 H retained in the mantle, we get a bulk mantle containing 0.07 to 0.09 %wt H_2O for the lowest
703 estimates of Brasser (2013) or Lunine et al. (2003); and between 2.1 and 2.7 % wt for the high
704 estimation of Dreibus and Wänke (1987). The latter is an upper bound and is enough for
705 saturating the mantle, and even to have vapor H_2O present, in which case the results of Médard
706 and Grove (2006) and Pommier et al. (2012) might be more relevant. Including the changes
707 induced by the extension of amphibole stability field in model such as the one of Elkins-Tanton
708 (2008) is then necessary to understand if an amphibole-richlayer can crystallize: as the magma
709 ocean crystallizes from bottom to top, it tends to concentrate volatiles towards the surface, and
710 increase their concentration (from 0.05 to 1% wt H_2O at 98 % crystallization in one of Elkins-
711 Tanton (2008) models). Therefore, even if the actual range of initial bulk water content is close
712 to that of Brasser (2013) or Lunine et al. (2003), the probability of Mars ever having crystallized
713 an amphibole-rich layer can be high by concentrating the water toward the upper mantle, but
714 have yet to be confirmed by proper thermodynamical modeling. As discussed in the previous
715 subsection, if the seismic record on Mars can get more precise and shows a probable existence
716 of an amphibole rich layer, then this would be an indicator that the initial water budget in early
717 Mars' mantle is higher than the most conservative estimations (Brasser, 2013) or that the
718 crystallization of the magma ocean lead to localize favorable conditions for amphibole
719 crystallization in the upper mantle (Elkins-Tanton, 2008). Furthermore, having the right
720 concentrations (0.1 - 1%wt) of water would extend the solidus of the martian mantle to higher
721 temperatures at depths around 100 km, up to 250 km. It would then tend to favor a more rapid
722 magma ocean crystallization, since the ΔT would be lower. Though this effect might be little,
723 given the rapid timescale for magma ocean crystallization on Mars (few millions years Elkins-

Tanton, 2008). Considering a higher initial water budget (around 1%wt), and a magma ocean crystallization process that can retain at least 50% of H, then the bulk concentration of water in the martian is high enough (0.5 %wt) for amphiboles to be stable in the upper mantle. These high water concentrations in a hot environment would tend to be in the melts and contribute to early Noachian volcanism (Brož et al., 2021). On the other hand, if the cooling rate is fast enough and the melts are trapped in this area of the mantle, then the formation of amphiboles will tend to remove water from the exchangeable reservoir, since the recycling of crust is very limited (Morschhauser et al., 2011). It would be possible then to remove water from the exchangeable reservoir as defined by Scheller et al. (2021) by early crystallization of amphiboles in the upper martian mantle.

4.6.3 Implications for volcanism and water loss of Mars

The water not retained in the mantle would go in forming the early atmosphere, where it can be lost. Some of the atmospheric water is lost by atmospheric loss (Kurokawa et al., 2014) and some by storage in surface hydrous minerals (Chassefière et al., 2013; Wernicke and Jakosky, 2021) The only source left of surface water is volcanism (e.g., Kiefer and Li, 2016; Xiao et al., 2012). The association of all the sources and sink of surface water preside the timing of Mars drying (Scheller et al., 2021). A full thermal history derived from early Mars (e.g. Xiao et al., 2012) to the current mantle (Plesa et al., 2018; Samuel et al., 2021) would be necessary to explain the ifs, when and where amphiboles might have crystallized. Furthermore, there is evidence of heterogeneous water storage on martian mantle (Barnes et al., 2020), and that the volcanism on Mars is dominated by mantle plume (Andrews-Hanna and Broquet, 2023). Localized higher concentration of water, either by initial heterogeneities in the mantle (Barnes et al., 2020)or some crustal recycling (Morschhauser et al., 2011)would therefore favor a local crystallization of amphiboles. In such a context, the mantle would be melting at higher temperature, only when a heat plume would go through it (Andrews-Hanna and Broquet, 2023), producing water rich melts. The presence of volatile elements dissolved in the melt will tend to

favor explosive volcanism (Cashman and Scheu, 2015; Gonnermann, 2015), while mafic melts with no volatile tend to favor effusive eruptions (Newcombe et al., 2020). In the absence of an amphibole-rich layer, then the volcanism would be less water-rich and more effusive. On Mars, explosive volcanism is rare compared to effusive events (Brož et al., 2021) and limited to Noachian times, while effusive volcanism with magmas undersaturated in water is the dominant volcanic regime during the Amazonian period (Kiefer and Li, 2016). The melting of an amphibole-rich assemblage can act as a source of volatile in the martian melts (e.g. Médard and Grove, 2006; Saha et al., 2018) and therefore the local variation in amphibole stability though time might explain, at least partly, the different volcanism types observed in Mars.

5 Conclusion

In summary, our study shows that relatively low water content in the Bulk Martian mantle stabilize amphiboles towards higher temperature and pressure. The composition of the martian mantle also plays a role, with compositional dependency comparable to those previously determined for the Earth, despite higher iron content and lower Mg # in the bulk silicate mars.

This stabilization of amphiboles happens in the upper mantle region and extends between 70 and 250 km depth, depending on the thermal profile chosen and the total alkali content. The presence of this layer leads to an increase of water storage capacity corresponding to a 400 m to 1.5 km increases in the Global Equivalent Layer, i.e. ~40 to ~ 1000 Earth Ocean mass added in water storage capacity, depending on the composition and thermal profile chosen. Seismic data are not yet sufficient to conclude as to the existence of such a layer in the current martian mantle. More seismic data from marsquakes could show the existence of a low S-wave velocity zone in the depths predicted by our model. In which case, this would be an indication that early mars accretion happened in a sufficiently wet environment to favor crystallization of hydrous minerals in the mantle. The presence of an amphibole-rich layer could then be an additional constraint on the thermal history of Mars and may lead to a changing of our understanding of

775 the crystallization of the magma ocean, or our understanding of the cooling rate of the martian
776 mantle and its relation to the long term drying of Mars. On a more local scale the presence of
777 deep hydrous mineral might account for part of the variability observed for the martian
778 volcanism, by favoring deep hydrous melting and therefore explosive basaltic volcanism.

779 References

780 Andrews-Hanna, J.C., Broquet, A., 2023. The history of global strain and geodynamics on Mars.
781 Icarus 115476. https://doi.org/10.1016/j.icarus.2023.115476
782 Barnes, J.J., McCubbin, F.M., Santos, A.R., Day, J.M.D., Boyce, J.W., Schwenzer, S.P., Ott, U., Franchi,
783 I.A., Messenger, S., Anand, M., Agee, C.B., 2020. Multiple early-formed water reservoirs
784 in the interior of Mars. Nat. Geosci. 13, 260–264. https://doi.org/10.1038/s41561-020-
785 0552-y
786 Bertka, C.M., Fei, Y., 1997. Mineralogy of the Martian interior up to core-mantle boundary
787 pressures. J. Geophys. Res. Solid Earth 102, 5251–5264.
788 https://doi.org/10.1029/96JB03270
789 Bibring, J.-P., Langevin, Y., Gendrin, A., Gondet, B., Poulet, F., Berthé, M., Soufflot, A., Arvidson, R.,
790 Mangold, N., Mustard, J., Drossart, P., the OMEGA team, 2005. Mars Surface Diversity as
791 Revealed by the OMEGA/Mars Express Observations. Science 307, 1576–1581.
792 https://doi.org/10.1126/science.1108806
793 Bibring, J.-P., Langevin, Y., Poulet, F., Gendrin, A., Gondet, B., Berthé, M., Soufflot, A., Drossart, P.,
794 Combes, M., Bellucci, G., Moroz, V., Mangold, N., Schmitt, B., OMEGA team, the, 2004.
795 Perennial water ice identified in the south polar cap of Mars. Nature 428, 627–630.
796 https://doi.org/10.1038/nature02461
797 Brasser, R., 2013. The Formation of Mars: Building Blocks and Accretion Time Scale. Space Sci.
798 Rev. 174, 11–25. https://doi.org/10.1007/s11214-012-9904-2
799 Breuer, D., Plesa, A.-C., Tosi, N., Grott, M., 2016. Water in the Martian interior—The
800 geodynamical perspective. Meteorit. Planet. Sci. 51, 1959–1992.
801 https://doi.org/10.1111/maps.12727
802 Brož, P., Bernhardt, H., Conway, S.J., Parekh, R., 2021. An overview of explosive volcanism on
803 Mars. J. Volcanol. Geotherm. Res. 409, 107125.
804 https://doi.org/10.1016/j.jvolgeores.2020.107125
805 Carr, M.H., Head, J.W., 2015. Martian surface/near-surface water inventory: Sources, sinks, and
806 changes with time: Martian water. Geophys. Res. Lett. 42, 726–732.
807 https://doi.org/10.1002/2014GL062464
808 Carter, L.B., Dasgupta, R., 2015. Hydrous basalt–limestone interaction at crustal conditions:
809 Implications for generation of ultracalcic melts and outflux of CO2 at volcanic arcs. Earth
810 Planet. Sci. Lett. 427, 202–214. https://doi.org/10.1016/j.epsl.2015.06.053
811 Cashman, K.V., Scheu, B., 2015. Chapter 25 - Magmatic Fragmentation, in: Sigurdsson, H. (Ed.),
812 The Encyclopedia of Volcanoes (Second Edition). Academic Press, Amsterdam, pp. 459–
813 471. https://doi.org/10.1016/B978-0-12-385938-9.00025-0
814 Chassefière, E., Langlais, B., Quesnel, Y., Leblanc, F., 2013. The fate of early Mars' lost water: The
815 role of serpentinization. J. Geophys. Res. Planets 118, 1123–1134.
816 https://doi.org/10.1002/jgre.20089
817 Clesi, V., Bouhifd, M.A., Bolfan-Casanova, N., Manthilake, G., Fabbrizio, A., Andrault, D., 2016.
818 Effect of H2O on metal–silicate partitioning of Ni, Co, V, Cr, Mn and Fe: Implications for

819 the oxidation state of the Earth and Mars. Geochim. Cosmochim. Acta 192, 97–121.
820 https://doi.org/10.1016/j.gca.2016.07.029
821 Condamine, P., Médard, E., 2014. Experimental melting of phlogopite-bearing mantle at 1 GPa:
822 Implications for potassic magmatism. Earth Planet. Sci. Lett. 397, 80–92.
823 https://doi.org/10.1016/j.epsl.2014.04.027
824 Condamine, P., Médard, E., Devidal, J.-L., 2016. Experimental melting of phlogopite-peridotite in
825 the garnet stability field. Contrib. Mineral. Petrol. 171, 95.
826 https://doi.org/10.1007/s00410-016-1306-0
827 Dasgupta, R., 2018. Volatile-bearing partial melts beneath oceans and continents–Where, how
828 much, and of what compositions? Am. J. Sci. 318, 141–165.
829 https://doi.org/10.2475/01.2018.06
830 Dasgupta, R., Aubaud, C., 2024. Major volatiles in the Earth's mantle beneath mid-ocean ridges
831 and intraplate ocean islands. *Treatise on Geochemistry*.
832 Ding, S., Dasgupta, R., Tsuno, K., 2014. Sulfur concentration of martian basalts at sulfide
833 saturation at high pressures and temperatures – Implications for deep sulfur cycle on
834 Mars. Geochim. Cosmochim. Acta 131, 227–246.
835 https://doi.org/10.1016/j.gca.2014.02.003
836 Dong, J., Fischer, R.A., Stixrude, L.P., Lithgow-Bertelloni, C.R., 2021. Constraining the Volume of
837 Earth's Early Oceans With a Temperature-Dependent Mantle Water Storage Capacity
838 Model. AGU Adv. 2. https://doi.org/10.1029/2020AV000323
839 Dong, J., Fischer, R.A., Stixrude, L.P., Lithgow-Bertelloni, C.R., Eriksen, Z.T., Brennan, M.C., 2022.
840 Water storage capacity of the martian mantle through time. Icarus 385, 115113.
841 https://doi.org/10.1016/j.icarus.2022.115113
842 Dreibus, G., Wänke, H., 1987. Volatiles on Earth and Mars: A comparison. Icarus 71, 225–240.
843 https://doi.org/10.1016/0019-1035(87)90148-5
844 Elkins-Tanton, L.T., 2008. Linked magma ocean solidification and atmospheric growth for Earth
845 and Mars. Earth Planet. Sci. Lett. 271, 181–191.
846 https://doi.org/10.1016/j.epsl.2008.03.062
847 Filiberto, J., Baratoux, D., Beaty, D., Breuer, D., Farcy, B.J., Grott, M., Jones, J.H., Kiefer, W.S., Mane,
848 P., McCubbin, F.M., Schwenzer, S.P., 2016. A review of volatiles in the Martian interior.
849 Meteorit. Planet. Sci. 51, 1935–1958. https://doi.org/10.1111/maps.12680
850 Filiberto, J., Dasgupta, R., Kiefer, W.S., Treiman, A.H., 2010a. High pressure, near-liquidus phase
851 equilibria of the Home Plate basalt Fastball and melting in the Martian mantle. Geophys.
852 Res. Lett. 37, 2010GL043999. https://doi.org/10.1029/2010GL043999
853 Filiberto, J., Musselwhite, D.S., Gross, J., Burgess, K., Le, L., Treiman, A.H., 2010b. Experimental
854 petrology, crystallization history, and parental magma characteristics of olivine-phyric
855 shergottite NWA 1068: Implications for the petrogenesis of "enriched" olivine-phyric
856 shergottites. Meteorit. Planet. Sci. 45, 1258–1270. https://doi.org/10.1111/j.1945-
857 5100.2010.01080.x
858 Fumagalli, P., Zanchetta, S., Poli, S., 2009. Alkali in phlogopite and amphibole and their effects
859 on phase relations in metasomatized peridotites: a high-pressure study. Contrib.
860 Mineral. Petrol. 158, 723–737. https://doi.org/10.1007/s00410-009-0407-4
861 Gonnermann, H.M., 2015. Magma Fragmentation. Annu. Rev. Earth Planet. Sci. 43, 431–458.
862 https://doi.org/10.1146/annurev-earth-060614-105206
863 Green, D.H., Hibberson, W.O., Kovács, I., Rosenthal, A., 2010. Water and its influence on the
864 lithosphere–asthenosphere boundary. Nature 467, 448–451.
865 https://doi.org/10.1038/nature09369
866 Green, D.H., Hibberson, W.O., Rosenthal, A., Kovács, I., Yaxley, G.M., Falloon, T.J., Brink, F., 2014.
867 Experimental Study of the Influence of Water on Melting and Phase Assemblages in the
868 Upper Mantle. J. Petrol. 55, 2067–2096. https://doi.org/10.1093/petrology/egu050

Grove, T., Chatterjee, N., Parman, S., Medard, E., 2006. The influence of H2O on mantle wedge melting. Earth Planet. Sci. Lett. 249, 74–89. https://doi.org/10.1016/j.epsl.2006.06.043
Hirschmann, M.M., Aubaud, C., Withers, A.C., 2005. Storage capacity of H2O in nominally anhydrous minerals in the upper mantle. Earth Planet. Sci. Lett. 236, 167–181. https://doi.org/10.1016/j.epsl.2005.04.022
Jakosky, B.M., 2021. Atmospheric Loss to Space and the History of Water on Mars. Annu. Rev. Earth Planet. Sci. 49, 71–93. https://doi.org/10.1146/annurev-earth-062420-052845
Keppler, H., 2006. Thermodynamics of Water Solubility and Partitioning. Rev. Mineral. Geochem. 62, 193–230. https://doi.org/10.2138/rmg.2006.62.9
Khan, A., Ceylan, S., van Driel, M., Giardini, D., Lognonné, P., Samuel, H., Schmerr, N.C., Stähler, S.C., Duran, A.C., Huang, Q., Kim, D., Broquet, A., Charalambous, C., Clinton, J.F., Davis, P.M., Drilleau, M., Karakostas, F., Lekic, V., McLennan, S.M., Maguire, R.R., Michaut, C., Panning, M.P., Pike, W.T., Pinot, B., Plasman, M., Scholz, J.-R., Widmer-Schnidrig, R., Spohn, T., Smrekar, S.E., Banerdt, W.B., 2021. Upper mantle structure of Mars from InSight seismic data. Science 373, 434–438. https://doi.org/10.1126/science.abf2966
Khan, A., Sossi, P.A., Liebske, C., Rivoldini, A., Giardini, D., 2022. Geophysical and cosmochemical evidence for a volatile-rich Mars. Earth Planet. Sci. Lett. 578, 117330. https://doi.org/10.1016/j.epsl.2021.117330
Kiefer, W.S., Li, Q., 2016. Water undersaturated mantle plume volcanism on present-day Mars. Meteorit. Planet. Sci. 51, 1993–2010. https://doi.org/10.1111/maps.12720
Knapmeyer-Endrun, B., Panning, M.P., Bissig, F., Joshi, R., Khan, A., Kim, D., Lekić, V., Tauzin, B., Tharimena, S., Plasman, M., Compaire, N., Garcia, R.F., Margerin, L., Schimmel, M., Stutzmann, É., Schmerr, N., Bozdağ, E., Plesa, A.-C., Wieczorek, M.A., Broquet, A., Antonangeli, D., McLennan, S.M., Samuel, H., Michaut, C., Pan, L., Smrekar, S.E., Johnson, C.L., Brinkman, N., Mittelholz, A., Rivoldini, A., Davis, P.M., LognonnÉ, P., Pinot, B., Scholz, J.-R., Stähler, S., Knapmeyer, M., van Driel, M., Giardini, D., Banerdt, W.B., 2021. Thickness and structure of the martian crust from InSight seismic data. Science 373, 438–443. https://doi.org/10.1126/science.abf8966
Kovács, I., Lenkey, L., Green, David.H., Fancsik, T., Falus, G., Kiss, J., Orosz, L., Angyal, J., Vikor, Z., 2017. The role of pargasitic amphibole in the formation of major geophysical discontinuities in the shallow upper mantle. Acta Geod. Geophys. 52, 183–204. https://doi.org/10.1007/s40328-016-0191-3
Kurokawa, H., Sato, M., Ushioda, M., Matsuyama, T., Moriwaki, R., Dohm, J.M., Usui, T., 2014. Evolution of water reservoirs on Mars: Constraints from hydrogen isotopes in martian meteorites. Earth Planet. Sci. Lett. 394, 179–185. https://doi.org/10.1016/j.epsl.2014.03.027
Lesne, P., Scaillet, B., Pichavant, M., Iacono-Marziano, G., Beny, J.-M., 2011. The H2O solubility of alkali basaltic melts: an experimental study. Contrib. Mineral. Petrol. 162, 133–151. https://doi.org/10.1007/s00410-010-0588-x
Locock, A.J., 2014. An Excel spreadsheet to classify chemical analyses of amphiboles following the IMA 2012 recommendations. Comput. Geosci. 62, 1–11. https://doi.org/10.1016/j.cageo.2013.09.011
Lodders, K., Fegley, B., 1997. An Oxygen Isotope Model for the Composition of Mars. Icarus 126, 373–394. https://doi.org/10.1006/icar.1996.5653
Lunine, J.I., Chambers, J., Morbidelli, A., Leshin, L.A., 2003. The origin of water on Mars. Icarus 165, 1–8. https://doi.org/10.1016/S0019-1035(03)00172-6
Mallik, A., Nelson, J., Dasgupta, R., 2015. Partial melting of fertile peridotite fluxed by hydrous rhyolitic melt at 2–3 GPa: implications for mantle wedge hybridization by sediment melt and generation of ultrapotassic magmas in convergent margins. Contrib. Mineral. Petrol. 169, 48. https://doi.org/10.1007/s00410-015-1139-2
Mandler, B.E., Grove, T.L., 2016. Controls on the stability and composition of amphibole in the Earth's mantle. Contrib. Mineral. Petrol. 171, 68. https://doi.org/10.1007/s00410-016-1281-5

Maurice, M., Dasgupta, R., Hassanzadeh, P., 2023. Redox Evolution of the Crystallizing Terrestrial Magma Ocean and Its Influence on the Outgassed Atmosphere. Planet. Sci. J. 4, 31. https://doi.org/10.3847/PSJ/acb2ca

McCubbin, F.M., Boyce, J.W., Srinivasan, P., Santos, A.R., Elardo, S.M., Filiberto, J., Steele, A., Shearer, C.K., 2016. Heterogeneous distribution of H2O in the Martian interior: Implications for the abundance of H2O in depleted and enriched mantle sources. Meteorit. Planet. Sci. 51, 2036–2060. https://doi.org/10.1111/maps.12639

Médard, E., Grove, T.L., 2006. Early hydrous melting and degassing of the Martian interior. J. Geophys. Res. 111, E11003. https://doi.org/10.1029/2006JE002742

Mitchell, A.L., Gaetani, G.A., O'Leary, J.A., Hauri, E.H., 2017. H2O solubility in basalt at upper mantle conditions. Contrib. Mineral. Petrol. 172, 85. https://doi.org/10.1007/s00410-017-1401-x

Morschhauser, A., Grott, M., Breuer, D., 2011. Crustal recycling, mantle dehydration, and the thermal evolution of Mars. Icarus 212, 541–558. https://doi.org/10.1016/j.icarus.2010.12.028

Mysen, B.R.O., Boettcher, A.L., 1975. Melting of a Hydrous Mantle: I. Phase Relations of Natural Peridotite at High Pressures and Temperatures with Controlled Activities of Water, Carbon Dioxide, and Hydrogen. J. Petrol. 16, 520–548. https://doi.org/10.1093/petrology/16.1.520

Newcombe, M.E., Plank, T., Zhang, Y., Holycross, M., Barth, A., Lloyd, A.S., Ferguson, D., Houghton, B.F., Hauri, E., 2020. Magma Pressure-Temperature-Time Paths During Mafic Explosive Eruptions. Front. Earth Sci. 8.

Niida, K., Green, D.H., 1999. Stability and chemical composition of pargasitic amphibole in MORB pyrolite under upper mantle conditions. Contrib. Mineral. Petrol. 135, 18–40. https://doi.org/10.1007/s004100050495

Ohtani, E., 2015. Hydrous minerals and the storage of water in the deep mantle. Chem. Geol. 418, 6–15. https://doi.org/10.1016/j.chemgeo.2015.05.005

O'Leary, J.A., Gaetani, G.A., Hauri, E.H., 2010. The effect of tetrahedral Al3+ on the partitioning of water between clinopyroxene and silicate melt. Earth Planet. Sci. Lett. 297, 111–120. https://doi.org/10.1016/j.epsl.2010.06.011

Pirard, C., Hermann, J., 2015. Experimentally determined stability of alkali amphibole in metasomatised dunite at sub-arc pressures. Contrib. Mineral. Petrol. 169, 1. https://doi.org/10.1007/s00410-014-1095-2

Plesa, A.-C., Padovan, S., Tosi, N., Breuer, D., Grott, M., Wieczorek, M.A., Spohn, T., Smrekar, S.E., Banerdt, W.B., 2018. The Thermal State and Interior Structure of Mars. Geophys. Res. Lett. 45, 12,198-12,209. https://doi.org/10.1029/2018GL080728

Pommier, A., Grove, T.L., Charlier, B., 2012. Water storage and early hydrous melting of the Martian mantle. Earth Planet. Sci. Lett. 333–334, 272–281. https://doi.org/10.1016/j.epsl.2012.03.030

Putak Juriček, M., Keppler, H., 2023. Amphibole stability, water storage in the mantle, and the nature of the lithosphere-asthenosphere boundary. Earth Planet. Sci. Lett. 608, 118082. https://doi.org/10.1016/j.epsl.2023.118082

Saha, S., Dasgupta, R., 2019. Phase Relations of a Depleted Peridotite Fluxed by a CO_2-H_2O Fluid—Implications for the Stability of Partial Melts Versus Volatile-Bearing Mineral Phases in the Cratonic Mantle. J. Geophys. Res. Solid Earth 124, 10089–10106. https://doi.org/10.1029/2019JB017653

Saha, S., Dasgupta, R., Tsuno, K., 2018. High Pressure Phase Relations of a Depleted Peridotite Fluxed by CO_2-H_2O-Bearing Siliceous Melts and the Origin of Mid-Lithospheric Discontinuity. Geochem. Geophys. Geosystems 19, 595–620. https://doi.org/10.1002/2017GC007233

Saha, S., Peng, Y., Dasgupta, R., Mookherjee, M., Fischer, K.M., 2021. Assessing the presence of volatile-bearing mineral phases in the cratonic mantle as a possible cause of mid-

lithospheric discontinuities. Earth Planet. Sci. Lett. 553, 116602. https://doi.org/10.1016/j.epsl.2020.116602
Samuel, H., Ballmer, M.D., Padovan, S., Tosi, N., Rivoldini, A., Plesa, A.-C., 2021. The Thermo-Chemical Evolution of Mars With a Strongly Stratified Mantle. J. Geophys. Res. Planets 126. https://doi.org/10.1029/2020JE006613
Samuel, H., Lognonné, P., Panning, M., Lainey, V., 2019. The rheology and thermal history of Mars revealed by the orbital evolution of Phobos. Nature 569, 523–527. https://doi.org/10.1038/s41586-019-1202-7
Sanloup, C., Jambon, A., Gillet, P., 1999. A simple chondritic model of Mars. Phys. Earth Planet. Inter. 112, 43–54. https://doi.org/10.1016/S0031-9201(98)00175-7
Schaefer, L., Elkins-Tanton, L.T., 2018. Magma oceans as a critical stage in the tectonic development of rocky planets. Philos. Trans. R. Soc. Math. Phys. Eng. Sci. 376, 20180109. https://doi.org/10.1098/rsta.2018.0109
Scheller, E.L., Ehlmann, B.L., Hu, R., Adams, D.J., Yung, Y.L., 2021. Long-term drying of Mars by sequestration of ocean-scale volumes of water in the crust. Science 372, 56–62. https://doi.org/10.1126/science.abc7717
Smrekar, S.E., Lognonné, P., Spohn, T., Banerdt, W.B., Breuer, D., Christensen, U., Dehant, V., Drilleau, M., Folkner, W., Fuji, N., Garcia, R.F., Giardini, D., Golombek, M., Grott, M., Gudkova, T., Johnson, C., Khan, A., Langlais, B., Mittelholz, A., Mocquet, A., Myhill, R., Panning, M., Perrin, C., Pike, T., Plesa, A.-C., Rivoldini, A., Samuel, H., Stähler, S.C., van Driel, M., Van Hoolst, T., Verhoeven, O., Weber, R., Wieczorek, M., 2019. Pre-mission InSights on the Interior of Mars. Space Sci. Rev. 215, 3. https://doi.org/10.1007/s11214-018-0563-9
Taylor, G.J., 2013. The bulk composition of Mars. Geochemistry 73, 401–420. https://doi.org/10.1016/j.chemer.2013.09.006
Till, C.B., Grove, T.L., Withers, A.C., 2012. The beginnings of hydrous mantle wedge melting. Contrib. Mineral. Petrol. 163, 669–688. https://doi.org/10.1007/s00410-011-0692-6
Trokhimovskiy, A., Fedorova, A., Korablev, O., Montmessin, F., Bertaux, J.-L., Rodin, A., Smith, M.D., 2015. Mars' water vapor mapping by the SPICAM IR spectrometer: Five martian years of observations. Icarus 251, 50–64. https://doi.org/10.1016/j.icarus.2014.10.007
Tsuno, K., Dasgupta, R., 2012. The effect of carbonates on near-solidus melting of pelite at 3GPa: Relative efficiency of H2O and CO2 subduction. Earth Planet. Sci. Lett. 319–320, 185–196. https://doi.org/10.1016/j.epsl.2011.12.007
Tsuno, K., Dasgupta, R., 2011. Melting phase relation of nominally anhydrous, carbonated pelitic-eclogite at 2.5–3.0 GPa and deep cycling of sedimentary carbon. Contrib. Mineral. Petrol. 161, 743–763. https://doi.org/10.1007/s00410-010-0560-9
Tumiati, S., Fumagalli, P., Tiraboschi, C., Poli, S., 2013. An Experimental Study on COH-bearing Peridotite up to 3·2 GPa and Implications for Crust–Mantle Recycling. J. Petrol. 54, 453–479. https://doi.org/10.1093/petrology/egs074
Von Seckendorff, V., O'Neill, H.St.C., 1993. An experimental study of Fe-Mg partitioning between olivine and orthopyroxene at 1173, 1273 and 1423 K and 1.6 GPa. Contrib. Mineral. Petrol. 113, 196–207. https://doi.org/10.1007/BF00283228
Wallace, M., Green, D.H., 1991. The effect of bulk rock composition on the stability of amphibole in the upper mantle: Implications for solidus positions and mantle metasomatism. Mineral. Petrol. 44, 1–19. https://doi.org/10.1007/BF01167097
Wänke, H., Dreibus, G., 1994. Chemistry and accretion history of Mars. Philos. Trans. R. Soc. Lond. Ser. Phys. Eng. Sci. 349, 285–293. https://doi.org/10.1098/rsta.1994.0132
Wernicke, L.J., Jakosky, B.M., 2021. Martian Hydrated Minerals: A Significant Water Sink. J. Geophys. Res. Planets 126, e2019JE006351. https://doi.org/10.1029/2019JE006351
Xiao, L., Huang, J., Christensen, P.R., Greeley, R., Williams, D.A., Zhao, J., He, Q., 2012. Ancient volcanism and its implication for thermal evolution of Mars. Earth Planet. Sci. Lett. 323–324, 9–18. https://doi.org/10.1016/j.epsl.2012.01.027

Yoshizaki, T., McDonough, W.F., 2020. The composition of Mars. Geochim. Cosmochim. Acta 273, 137–162. https://doi.org/10.1016/j.gca.2020.01.011

.

Supplementary Materials to "Water Storage in Hydrous Minerals in the Shallow Martian Mantle"

Vincent Clesi, Rajdeep Dasgupta

S.1 Determining the amphibole modal share

In the main text we use a parameterized relationship that yield the modal share of amphibole that can crystallize as a function of composition. This relationship is purely statistical, though grounded in previous effect known to affect the amphibole crystallization. If we follow Saha et al. (2021) the main controller are temperature, calcium content and the ratio of total alkali. If we add pressure to the mix, then we get the following equation:

$$\%wtAmph = aT + b\chi_{CaO}^{Bulk} + c\frac{\chi_{Na_2O}^{bulk}+\chi_{K_2O}^{bulk}}{\chi_{H_2O}^{bulk}} + dP \quad \text{S.1}$$

The parameters a, b, c and d are minimized by a mutliple linear least square minimization of the package numpy (linalg.lstsq). The fitting is performed on a reduced dataset, using only experiments where the modal share is different than 0, otherwise a large error is introduced in the parameterization. After fitting and recalculation, we obtain the results presented in Figure S.2, plotted against the different variables of Equation S.1. As seen in the figure, the predictive power of Equation S.1 is pretty low, hence the decision to take into account the entire composition of the bulk experiments in the equation presented in the main text. The equation presented in the main text has a better predictive content (See Figure 4 in the main text) despite its limitation for the higher values of amphiboles modal share. We use in the main text the maximum amphibole content.

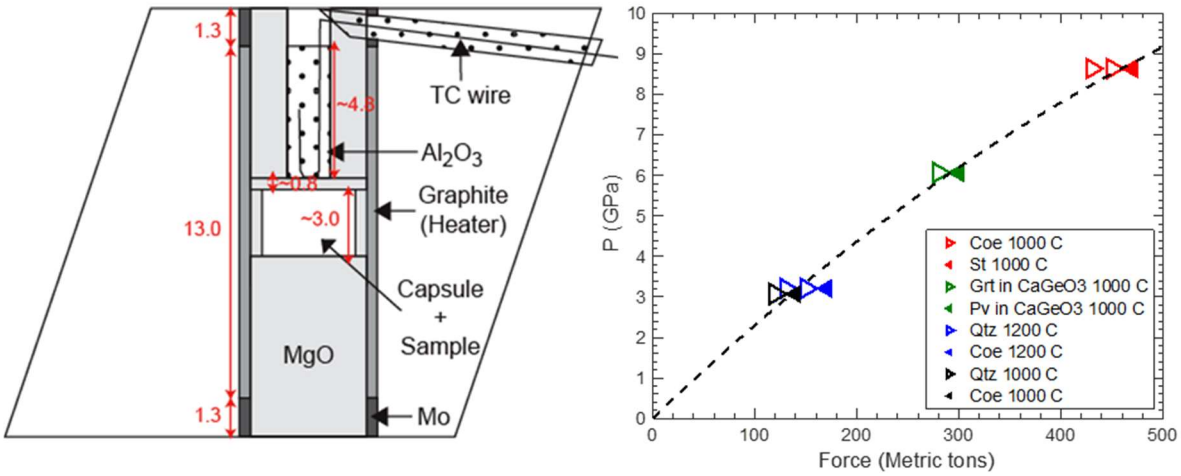

Figure S.1: **Left:** Schematics of the 18/12 apparatus in multi-anvil experiments at 4 GPa. **Right:** Calibration curve of the 18/12 mutli-anvil apparatus on the 100 ton Walker type press at Rice experimental petrology lab.

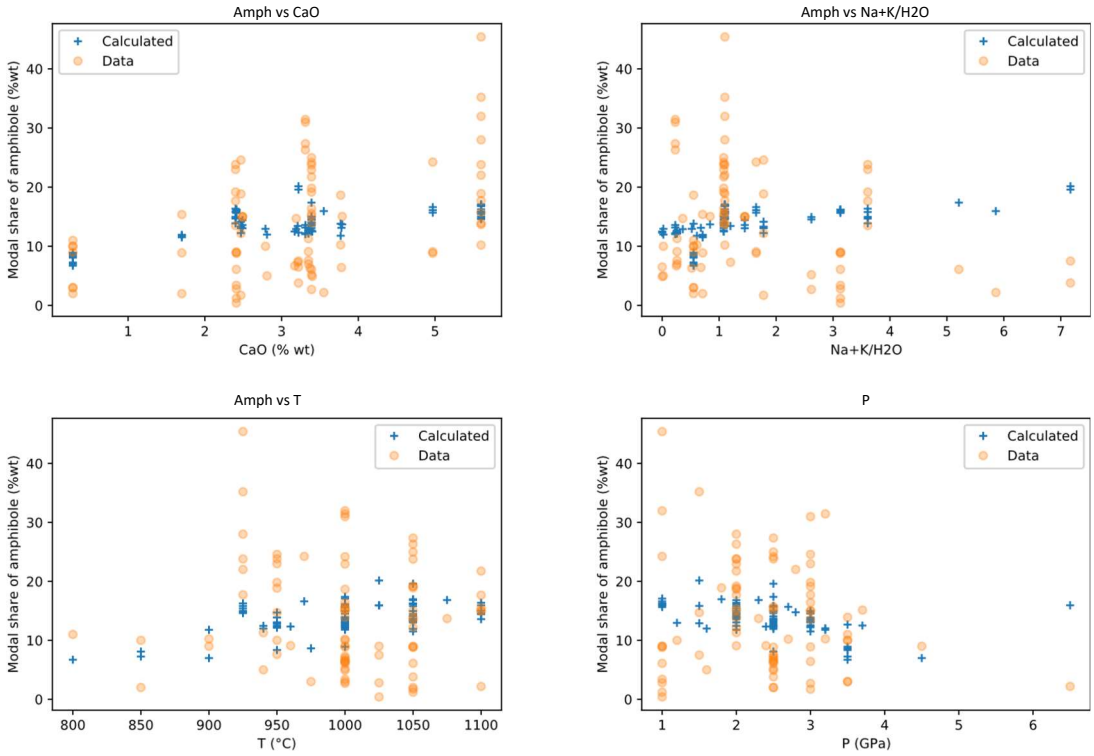

Figure S.2: Plot of the modal share of amphibole (%wt) as a function of CaO content (top left), $\frac{\chi_{Na_2O}^{bulk}+\chi_{K_2O}^{bulk}}{\chi_{H_2O}^{bulk}}$ (top right), temperature (bottom left) and pressure (bottom right). The blue crosses are the value obtained using Equation S.1, and the orange circles are the actual values from the dataset of Saha et al. (2021).

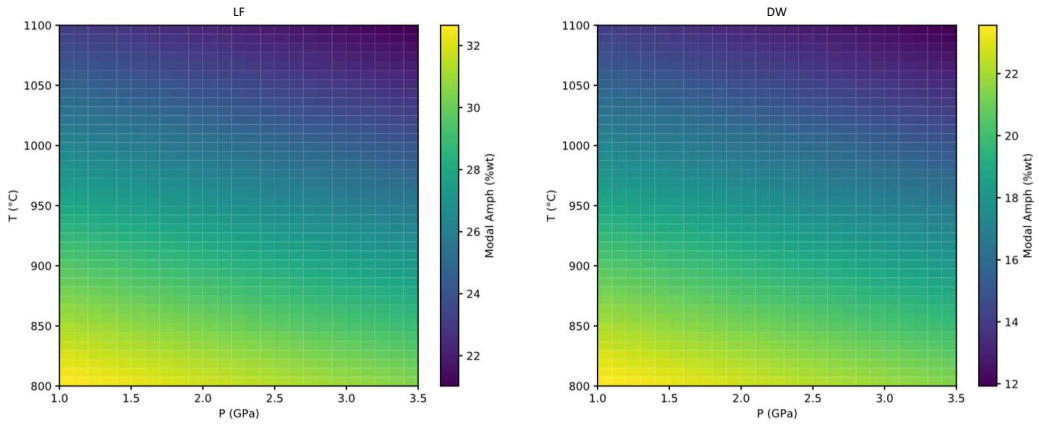

Figure S.3: Figure showing the modal share of amphibole for LF (left) and DW (right) compositions as a function of P and T as obtained by Equation 6(Figure 4, main text). The modal proportion are then used to calculate the modal share of amphiboles in the martian mantle presented in Figure 6 (main text) for the thermal profiles presented in Figure 5 (main text)..

References

Sriparna Saha, Ye Peng, Rajdeep Dasgupta, Mainak Mookherjee, and Karen M. Fischer. Assessing the presence of volatile-bearing mineral phases in the cratonic mantle as a possible cause of mid-lithospheric discontinuities. *Earth and Planetary Science Letters*, 553: 116602, January 2021. ISSN 0012821X. doi: 10.1016/j.epsl.2020.116602. URL https://linkinghub.elsevier.com/retrieve/pii/S0012821X2030546X.

Table	Legend
S.1.	Olivine compositions for starting material LF obtained by EPMA analysis
S.2.	Olivine compositions for starting material DW obtained by EPMA analysis
S.3.	Orthopyroxene compositions for starting material LF obtained by EPMA analysis
S.4.	Orthopyroxene compositions for starting material DW obtained by EPMA analysis
S.5.	Clinopyroxene compositions for starting material LF obtained by EPMA analysis
S.6.	Clinopyroxene compositions for starting material DW obtained by EPMA analysis
S.7.	Garnet compositions for starting material LF obtained by EPMA analysis
S.8.	Garnet compositions for starting material DW obtained by EPMA analysis

	T142-DW	1σ	T143-DW	1σ	T146-DW	1σ	T148-DW	1σ	T150-DW	1σ	T151-DW	1σ	T152-DW
SiO_2	38.47	0.33	38.00	0.99	38.47	0.69	38.02	0.73	37.90	1.79	38.52	0.78	38.56
TiO_2	0.02	0.02	0.02	0.03	0.01	0.02	0.01	0.02	0.03	0.02	0.02	0.02	0.03
Al_2O_3	0.05	0.11	0.26	0.78	0.10	0.19	0.16	0.47	0.20	0.35	0.14	0.32	0.01
FeO	23.23	1.00	24.28	1.74	23.58	0.35	22.36	0.71	24.71	0.49	22.26	1.02	23.19
MnO	0.41	0.02	0.47	0.04	0.40	0.03	0.44	0.03	0.31	0.04	0.34	0.02	0.36
MgO	37.32	1.12	37.05	1.34	36.70	0.78	37.48	0.86	35.76	0.90	38.86	0.83	36.63
CaO	0.06	0.02	0.08	0.04	0.10	0.03	0.09	0.03	0.06	0.06	0.05	0.01	0.07
Na_2O	0.02	0.02	0.01	0.02	0.05	0.07	0.02	0.02	0.00	0.01	0.02	0.02	0.02
K_2O	0.01	0.01	0.01	0.01	0.01	0.01	0.00	0.00	0.02	0.02	0.00	0.00	0.00
Total	99.59		100.19		99.44		98.58		99.00		100.21		98.87

Table S2

1σ	T153-DW	1σ	MA290	1σ	M295	1σ	MA298	1σ	MA303	1σ
0.51	38.54	0.97	36.46	0.50	38.90	0.44	39.18	0.41	39.77	0.43
0.03	0.02	0.03	0.04	0.01	0.02	0.02	0.02	0.02	0.02	0.02
0.02	0.02	0.01	0.02	0.02	0.01	0.01	0.01	0.01	0.02	0.02
0.76	23.32	0.24	23.49	1.16	20.76	0.69	21.09	0.71	21.16	0.72
0.03	0.42	0.03	0.30	0.03	0.36	0.03	0.36	0.02	0.38	0.03
0.92	38.28	0.41	39.02	1.12	41.29	0.73	37.17	0.87	38.84	0.89
0.02	0.11	0.02	0.05	0.03	0.06	0.01	0.06	0.01	0.07	0.02
0.03	0.01	0.01	0.02	0.02	0.02	0.02	0.04	0.06	0.04	0.02
0.00	0.00	0.00	0.01	0.01	0.01	0.01	0.04	0.09	0.01	0.01
	100.72		99.42		101.44		97.98		100.32	

	T142-LF	1σ	T143-LF	1σ	T146-LF	1σ	T148-LF	1σ	T150-LF	1σ	T151-LF	1σ	T152-LF
SiO_2	38.59	1.12	38.22	0.37	37.73	0.34	39.10	0.42	38.20	0.85	37.11	0.85	38.95
TiO_2	0.02	0.02	0.01	0.01	0.02	0.02	0.01	0.01	0.02	0.02	0.04	0.02	0.02
Al_2O_3	0.20	0.55	0.04	0.01	0.06	0.09	0.02	0.01	0.03	0.07	0.53	0.07	0.07
FeO	21.87	1.25	20.68	0.73	23.40	0.70	22.47	0.47	24.11	2.24	21.98	2.24	21.87
MnO	0.37	0.05	0.37	0.02	0.39	0.03	0.37	0.03	0.34	0.04	0.36	0.04	0.30
MgO	38.97	1.96	40.94	0.85	37.67	0.96	38.25	0.35	37.36	2.50	37.31	2.50	39.30
CaO	0.16	0.41	0.06	0.02	0.09	0.02	0.10	0.01	0.04	0.02	0.12	0.02	0.06
Na_2O	0.06	0.19	0.03	0.04	0.02	0.01	0.02	0.02	0.01	0.02	0.08	0.02	0.06
K_2O	0.02	0.02	0.01	0.01	0.01	0.01	0.00	0.00	0.00	0.00	0.00	0.00	0.00
Total	100.26		100.35		99.39		100.35		100.12		97.53		100.63

Table S1

1σ	T153-LF	1σ	MA293	1σ	MA297	1σ	MA300	1σ	MA302	1σ
0.39	38.39	0.45	38.60	0.66	39.38	0.30	39.01	0.47	39.14	0.57
0.02	0.01	0.01	0.03	0.02	0.03	0.02	0.02	0.01	0.02	0.02
0.17	0.05	0.04	0.01	0.01	0.13	0.37	0.01	0.01	0.03	0.02
1.02	21.92	0.27	23.07	0.94	21.45	0.43	21.50	0.46	20.55	0.62
0.03	0.32	0.01	0.29	0.02	0.30	0.02	0.29	0.05	0.30	0.03
0.90	39.81	0.38	37.14	0.70	38.02	1.02	38.74	0.40	40.11	0.89
0.03	0.10	0.02	0.05	0.01	0.06	0.05	0.03	0.01	0.06	0.01
0.04	0.01	0.01	0.30	0.51	0.06	0.02	0.02	0.02	0.06	0.02
0.00	0.00	0.00	0.00	0.01	0.01	0.01	0.00	0.01	0.01	0.01
	100.61		99.50		99.44		99.63		100.27	

	T142-LF	1σ	T143-LF	1σ	T146-LF	1σ	T148-LF	1σ	T150-LF	1σ	T151-LF	1σ	T152-LF
SiO_2	54.67	0.73	54.31	0.61	53.70	0.49	54.78	0.38	55.32	0.48	54.92	0.48	55.28
TiO_2	0.05	0.03	0.05	0.03	0.07	0.03	0.10	0.03	0.06	0.03	0.13	0.03	0.14
Al_2O_3	1.43	0.27	1.63	0.20	2.39	0.26	3.00	0.46	1.51	0.14	1.52	0.14	1.88
FeO	14.25	0.78	12.93	0.37	14.15	0.40	13.40	0.41	13.74	0.75	14.37	0.75	13.12
MnO	0.41	0.11	0.39	0.02	0.43	0.11	0.35	0.02	0.33	0.06	0.39	0.06	0.32
MgO	28.21	0.95	29.32	0.36	27.25	0.59	27.30	0.41	28.50	0.75	27.79	0.75	28.43
CaO	0.90	0.47	0.92	0.06	1.14	0.10	1.26	0.12	0.62	0.05	0.85	0.05	0.95
Na_2O	0.12	0.06	0.19	0.02	0.28	0.05	0.24	0.03	0.09	0.03	0.18	0.03	0.30
K_2O	0.01	0.02	0.01	0.01	0.01	0.01	0.01	0.01	0.00	0.00	0.01	0.00	0.02
Total	100.07		99.75		99.44		100.43		100.17		100.16		100.44

Table S3

1σ	T153-LF	1σ	MA293	1σ	MA297	1σ	MA300	1σ	MA302	1σ
0.34	53.72	0.49	55.10	0.90	56.30	0.50	54.89	0.42	56.24	0.44
0.02	0.10	0.04	0.12	0.04	0.11	0.03	0.08	0.04	0.06	0.03
0.05	3.55	0.26	1.03	0.10	1.12	0.10	0.89	0.22	1.19	0.06
0.14	13.32	0.23	13.62	0.46	12.64	0.41	12.60	0.28	11.99	0.19
0.03	0.34	0.02	0.29	0.02	0.31	0.03	0.33	0.03	0.30	0.02
0.26	27.78	0.39	28.09	0.68	28.17	0.49	28.54	0.37	28.06	0.48
0.05	1.23	0.08	0.84	0.24	0.81	0.09	0.60	0.08	0.92	0.05
0.07	0.25	0.05	0.32	0.09	0.33	0.08	0.25	0.07	0.34	0.04
0.02	0.01	0.01	0.01	0.02	0.01	0.02	0.02	0.01	0.01	0.01
	100.29		99.41		99.80		98.20		99.11	

	T142-DW	1σ	T143-DW	1σ	T146-DW	1σ	T148-DW	1σ	T150-DW	1σ	T151-DW	1σ	T152-DW
SiO_2	54.69	0.69	54.02	0.65	53.25	0.75	53.68	0.74	54.15	1.78	54.51	0.60	55.52
TiO_2	0.06	0.04	0.07	0.04	0.09	0.03	0.10	0.04	0.02	0.02	0.08	0.02	0.14
Al_2O_3	2.15	0.68	2.89	0.61	3.14	0.23	2.87	0.82	0.99	0.27	1.96	0.19	1.45
FeO	15.04	0.57	14.29	1.01	15.02	0.44	13.85	0.82	15.26	1.29	14.27	0.12	13.75
MnO	0.40	0.06	0.46	0.05	0.37	0.02	0.43	0.03	0.28	0.08	0.38	0.03	0.39
MgO	26.71	0.81	26.62	1.88	26.52	0.59	25.94	0.74	28.84	0.57	27.93	0.15	26.73
CaO	0.74	0.10	1.57	2.12	1.11	0.05	1.30	0.17	0.37	0.12	0.81	0.06	1.02
Na_2O	0.07	0.04	0.16	0.18	0.11	0.04	0.11	0.02	0.04	0.03	0.21	0.04	0.12
K_2O	0.01	0.02	0.00	0.00	0.01	0.01	0.00	0.00	0.01	0.01	0.00	0.01	0.00
Total	99.86		100.08		99.63		98.28		99.95		100.13		99.11

Table S4

1σ	T153-DW	1σ	MA290	1σ	M295	1σ	MA298	1σ	MA303	1σ
0.56	53.71	0.70	54.08	0.56	55.30	0.51	55.79	0.61	56.55	0.47
0.04	0.10	0.03	0.09	0.03	0.07	0.03	0.07	0.03	0.05	0.02
0.06	3.07	0.26	0.59	0.13	1.45	0.11	1.09	0.06	1.15	0.07
0.18	13.94	0.21	14.23	0.83	12.02	0.28	11.58	0.26	12.07	0.43
0.02	0.40	0.04	0.35	0.02	0.37	0.02	0.38	0.03	0.37	0.02
0.36	27.36	0.32	29.15	0.57	30.64	0.50	28.05	0.72	28.11	0.65
0.04	1.31	0.07	0.60	0.08	1.01	0.05	0.90	0.06	1.17	0.08
0.02	0.12	0.03	0.13	0.02	0.11	0.03	0.41	0.32	0.16	0.03
0.00	0.01	0.01	0.01	0.01	0.01	0.02	0.01	0.01	0.02	0.01
	100.01		99.23		100.98		98.27		99.65	

	T142-LF	1σ	T143-LF	1σ	T146-LF	1σ	T148-LF	1σ	T150-LF	1σ	T151-LF	1σ	T152-LF
SiO_2	52.05	2.57	52.74	0.32	51.31	3.17	53.53	0.48	53.49	0.21	54.05	0.21	54.61
TiO_2	0.19	0.16	0.10	0.04	0.22	0.22	0.29	0.05	0.08	0.05	0.32	0.05	0.32
Al_2O_3	3.54	2.79	3.36	0.18	4.20	3.20	5.66	0.34	2.46	0.35	3.15	0.35	4.98
FeO	12.05	2.49	9.70	0.48	13.95	4.12	7.85	0.37	8.76	0.36	7.94	0.36	7.74
MnO	0.29	0.08	0.27	0.03	0.50	0.25	0.27	0.03	0.26	0.05	0.31	0.05	0.26
MgO	15.26	2.18	15.13	0.35	19.56	4.61	15.29	0.49	15.57	1.46	15.47	1.46	15.43
CaO	12.85	3.57	15.87	0.69	7.63	6.49	15.86	0.56	17.19	1.61	17.27	1.61	14.64
Na_2O	2.53	0.74	2.27	0.22	1.52	1.24	1.97	0.09	1.75	0.29	1.60	0.29	2.90
K_2O	0.09	0.13	0.01	0.01	0.10	0.25	0.00	0.00	0.01	0.01	0.02	0.01	0.01
Total	98.85		99.44		98.98		100.74		99.55		100.11		100.87

Table S5

1σ	T153-LF	1σ	MA293	1σ	MA297	1σ	MA300	1σ	MA302	1σ
0.54	52.27	0.32	54.92	0.79	54.70	0.17	54.29	0.45	55.12	0.70
0.03	0.28	0.03	0.36	0.05	0.10	0.07	0.31	0.10	0.21	0.04
0.28	5.80	0.13	4.17	0.27	2.52	0.08	4.95	0.28	4.12	0.17
0.58	7.99	0.21	8.32	0.19	12.47	1.00	7.13	0.33	7.66	0.51
0.02	0.25	0.03	0.27	0.01	0.30	0.03	0.25	0.04	0.28	0.04
1.03	15.10	0.17	15.64	1.44	19.39	3.83	13.43	0.41	15.48	0.35
1.13	16.06	0.26	12.81	1.31	8.42	2.23	15.35	1.19	13.82	0.48
0.19	2.15	0.06	2.93	0.26	1.66	0.72	3.27	0.21	2.63	0.16
0.02	0.01	0.01	0.00	0.01	0.01	0.01	0.02	0.01	0.01	0.01
	99.90		99.42		99.55		99.00		99.32	

	T142-DW	1σ	T143-DW	1σ	T146-DW	1σ	T148-DW	1σ	T150-DW	1σ	T151-DW	1σ	T152-DW
SiO_2	53.16	0.97	52.87	0.50	52.74	0.39	52.23	0.33	52.76	0.36	52.50	0.76	54.67
TiO_2	0.14	0.06	0.17	0.06	0.23	0.03	0.21	0.10	0.15	0.05	0.25	0.01	0.27
Al_2O_3	3.01	0.89	3.84	0.71	4.21	0.18	3.79	0.10	2.58	0.06	3.79	0.04	2.86
FeO	9.95	0.78	9.12	0.34	8.78	0.39	8.92	1.17	9.28	0.24	8.68	0.21	7.49
MnO	0.36	0.05	0.36	0.04	0.29	0.03	0.38	0.03	0.31	0.02	0.33	0.00	0.31
MgO	14.58	0.47	15.02	0.33	14.14	0.28	15.68	0.11	16.30	2.61	14.78	0.26	15.27
CaO	17.60	1.14	17.30	0.59	17.56	0.50	16.06	1.29	16.48	2.56	16.31	0.01	17.70
Na_2O	1.28	0.35	1.42	0.18	1.30	0.07	0.94	0.09	0.99	0.34	2.61	0.07	1.31
K_2O	0.01	0.04	0.00	0.01	0.01	0.01	0.00	0.00	0.01	0.00	0.01	0.01	0.00
Total	100.09		100.11		99.26		98.19		98.86		99.24		99.86

Table S6

1σ	T153-DW	1σ	MA290	1σ	M295	1σ	MA298	1σ	MA303	1σ
0.46	52.77	0.39	53.30	0.15	54.02	0.51	53.77	1.75	55.34	0.35
0.04	0.21	0.03	0.26	0.06	0.13	0.04	0.19	0.05	0.08	0.03
0.12	4.19	0.23	3.56	0.35	2.04	0.17	3.56	1.55	2.14	0.08
0.18	8.26	0.26	7.89	0.86	6.25	0.47	5.13	1.95	7.14	0.50
0.02	0.32	0.01	0.27	0.02	0.30	0.03	0.33	0.22	0.33	0.03
0.11	16.28	0.45	15.54	0.92	17.92	0.26	15.95	1.83	16.38	0.29
0.32	17.06	0.57	15.75	0.60	18.94	0.56	16.88	1.82	16.82	0.78
0.04	1.03	0.06	2.07	0.23	0.67	0.06	1.79	0.39	1.08	0.05
0.00	0.01	0.01	0.02	0.02	0.01	0.02	0.01	0.01	0.01	0.01
	100.12		98.66		100.28		97.61		99.32	

	T146-LF	1σ	T148-LF	1σ	T151-LF	1σ	T152-LF	1σ	MA293	1σ	MA297	1σ	MA300
SiO_2	40.25	0.35	40.98	1.46	41.02	0.59	41.47	0.87	38.81	1.58	41.22	0.35	41.26
TiO_2	0.21	0.05	0.41	0.20	0.37	0.07	0.30	0.05	0.36	0.13	0.38	0.11	0.68
Al_2O_3	22.00	0.25	22.39	0.93	20.89	0.64	22.54	0.55	23.70	1.92	21.93	0.29	19.35
FeO	16.66	0.23	15.15	0.48	16.88	0.44	15.87	0.44	17.10	0.23	16.04	0.33	17.97
MnO	0.92	0.03	0.68	0.12	0.91	0.04	0.76	0.04	0.69	0.07	0.74	0.07	0.68
MgO	14.34	0.44	14.81	0.32	14.85	0.78	15.77	0.57	15.64	0.36	15.28	0.47	13.16
CaO	6.25	0.28	5.73	0.96	5.52	0.58	4.41	0.34	3.70	0.47	3.87	0.19	5.52
Na_2O	0.02	0.01	0.11	0.10	0.10	0.05	0.08	0.04	0.12	0.06	0.13	0.09	0.34
K_2O	0.01	0.01	0.03	0.04	0.02	0.01	0.01	0.01	0.01	0.01	0.01	0.01	0.01
Total	100.64		100.30		100.55		101.22		100.13		99.60		98.97

Table S7

1σ	MA302	1σ
1.66	41.54	0.37
0.15	0.66	0.21
1.58	21.36	0.50
0.41	16.24	1.28
0.08	0.57	0.09
1.08	15.48	0.98
0.94	3.92	0.21
0.21	0.11	0.03
0.01	0.01	0.01
	99.90	

	T146-DW	1σ	T148-DW	1σ	T150-DW	1σ	T151-DW	1σ	T152-DW	1σ	T153-DW	1σ	MA290
SiO_2	40.60	0.81	41.74	1.05	43.39	1.20	40.57	1.12	41.33	0.32	41.13	0.27	39.22
TiO_2	0.19	0.04	0.34	0.12	0.11	0.02	0.19	0.05	0.37	0.07	0.22	0.04	0.52
Al_2O_3	21.58	0.48	21.32	0.85	16.64	1.19	21.70	1.50	21.17	0.32	22.66	0.32	21.21
FeO	16.45	0.39	15.42	0.28	17.84	0.53	16.94	0.66	15.87	0.18	15.19	0.18	19.53
MnO	0.88	0.05	0.95	0.06	0.86	0.04	0.67	0.09	0.89	0.03	0.83	0.03	0.95
MgO	14.06	0.57	14.65	0.80	17.42	0.27	15.13	0.31	13.83	0.40	14.90	0.27	12.65
CaO	6.09	0.42	5.90	0.59	3.87	0.44	4.69	0.40	5.26	0.28	6.08	0.25	4.96
Na_2O	0.04	0.02	0.02	0.02	0.03	0.04	0.08	0.10	0.03	0.01	0.02	0.02	0.19
K_2O	0.01	0.01	0.01	0.01	0.00	0.00	0.01	0.02	0.00	0.01	0.00	0.01	0.01
Total	99.90		100.35		100.16		99.98		98.75		101.03		99.23

Table S8

1σ	M295	1σ	MA298	1σ	MA303	1σ
0.48	40.47	0.38	40.99	0.41	41.85	0.49
0.29	0.28	0.07	0.22	0.04	0.33	0.16
0.95	24.04	0.45	21.08	0.18	21.72	0.63
1.86	14.12	0.38	17.23	0.62	14.69	0.51
0.10	0.87	0.06	0.84	0.04	0.74	0.08
1.72	16.04	0.60	12.93	0.46	15.48	0.64
0.36	5.64	0.29	4.75	0.34	4.86	0.52
0.07	0.08	0.07	0.05	0.02	0.07	0.03
0.01	0.02	0.03	0.01	0.01	0.01	0.01
	101.56		98.10		99.74	